A Discontinuous Galerkin Method for Simulating 3D Seismic Wave Propagation in Nonlinear Rock Models: Verification and Application to the 2015 M_w 7.8 Gorkha Earthquake

Zihua Niu[1], Alice-Agnes Gabriel[2,1], Sebastian Wolf[3], Thomas Ulrich[1], Vladimir Lyakhovsky[4], Heiner Igel[1]

[1]Department of Earth and Environmental Sciences, Ludwig-Maximilians-Universität München, Munich, Germany
[2]Scripps Institution of Oceanography, UC San Diego, La Jolla, CA, USA
[3]Technical University of Munich, Munich, Germany
[4]Geological Survey of Israel, Jerusalem 9692100, Israel

Key Points:

- We propose and verify a 3D discontinuous Galerkin method for nonlinear seismic wave propagation on high-performance computing systems.
- The 2015 M_w 7.8 Gorkha earthquake simulations show co-seismic wave speed reductions from <0.01% to >50%, varying with fault slip and geology.
- The nonlinear model captures low-frequency ground motion amplification in soft sediments, highlighting key effects for seismic hazard analysis.

Abstract

The nonlinear mechanical responses of rocks and soils to seismic waves play an important role in earthquake physics, influencing ground motion from source to site. Continuous geophysical monitoring, such as ambient noise interferometry, has revealed co-seismic wave speed reductions extending tens of kilometers from earthquake sources. However, the mechanisms governing these changes remain challenging to model, especially at regional scales. Using a nonlinear damage model constrained by laboratory experiments, we develop and apply an open-source 3D discontinuous Galerkin method to simulate regional co-seismic wave speed changes during the 2015 M_w7.8 Gorkha earthquake. We find pronounced spatial variations of co-seismic wave speed reduction, ranging from <0.01% to >50%, particularly close to the source and within the Kathmandu Basin. The most significant reduction occurs within the sedimentary basin and varies with basin depths, while wave speed reductions correlate with the fault slip distribution near the source. By comparing ground motions from simulations with elastic, viscoelastic, elastoplastic, and nonlinear damage rheologies, we demonstrate that the nonlinear damage model effectively captures low-frequency ground motion amplification due to strain-dependent wave speed reductions in soft sediments. We verify the accuracy of our approach through comparisons with analytical solutions and assess its scalability on high-performance computing systems. The model shows near-linear strong and weak scaling up to 2048 nodes, enabling efficient large-scale simulations. Our findings provide a physics-based framework to quantify nonlinear earthquake effects and emphasize the importance of damage-induced wave speed variations for seismic hazard assessment and ground motion predictions.

Plain Language Summary

Earthquakes cause significant changes in the mechanical properties of rocks and soils, including reductions in seismic wave speeds. These changes, recorded over the past two decades using advanced monitoring techniques, such as ambient noise analysis, reveal valuable information about underground conditions. However, existing models cannot fully capture the complex nonlinear behavior of rocks and soils during an earthquake from source to site. To address this, we extend SeisSol, an open-source software for simulating seismic waves, to model 3D nonlinear wave propagation. We demonstrate the efficient execution of the code on powerful computers. This enhancement allows us to study co-seismic wave speed changes while accounting for complex fault geometry and surface topography. We apply this tool to the 2015 M_w Gorkha, Nepal, earthquake and find significant variations in wave speed reductions, ranging from less than 0.01% to over 50%, with the largest reductions concentrated in sedimentary basins. Comparisons with other models demonstrate that the nonlinear damage model employed in this study effectively captures the amplification of low-frequency ground motions by soft sediments, a key factor in understanding earthquake impacts. These insights improve our ability to assess seismic hazards and guide the design of infrastructure better equipped to withstand earthquakes.

1 Introduction

Large earthquakes generate strong ground motions that pose a significant threat to civil structures and human life (Ben-Zion et al., 2022). Physics-based models of rocks and soils are essential for simulating potential ground motions from earthquakes in numerical simulations that can account for the spatial heterogeneity and complex surface topography of the Earth's lithosphere (Cui et al., 2010; Taufiqurrahman et al., 2022; Roten et al., 2023). Linear models have successfully explained key phenomena in seismic wave propagation, such as wave field amplification in soft sediments (Moczo and Bard, 1993; van Ginkel et al., 2022), directivity effects of large earthquakes (Boatwright and Boore, 1982; Roten et al., 2014; Wollherr et al., 2019), and resonance in near-surface structures, including surface topography (Lee et al., 2009; Hartzell et al., 2014) and sedimentary basins (Castellaro and Musinu, 2023).

In recent decades, nonlinear mechanical responses of rocks to seismic waves have been widely observed, covering distances from a few kilometers to over one hundred kilometers from the source (Sens-Schönfelder and Wegler, 2006; Gassenmeier et al., 2016; Lu and Ben-Zion, 2022). Temporal variations in seismic wave speeds during and after earthquakes have been observed using techniques such as repeating earthquakes (Poupinet et al., 1984; Bokelmann and Harjes, 2000; Schaff and Beroza, 2004), cross-correlation of the ambient noise or aftershock recordings between seismic station pairs (Sens-Schönfelder and Wegler, 2006; Brenguier et al., 2008; Qiu et al., 2020), and auto-correlation of data at individual stations (Bonilla et al., 2019; Qin et al., 2020; Li and Ben-Zion, 2023). In these observations, rocks typically exhibit a rapid co-seismic reduction in seismic wave speeds, followed by long-term recovery (Gassenmeier et al., 2016). Measured magnitudes of such co-seismic wave speed reduction range from less than 1% up to over 10%, depending on factors such as rock type, distance from the source, depth of interests, and the temporal resolution of the monitoring technique (Brenguier et al., 2014; Wang et al., 2021). Notably, auto-correlation analyses at single stations reveal that co-seismic reductions in wave speed up to 8% are possible at depths between 1 km and 3 km within 20 minutes after an earthquake (Bonilla and Ben-Zion, 2021). Co-seismic wave speed changes under dynamic perturbation are sensitive to rheology, ambient stress, and thermal and hydraulic conditions (Manogharan et al., 2022; Lu and Ben-Zion, 2022). Such changes are potentially new observables that can be extracted from seismic waves to probe subsurface structure and rheology. However, observations of co-seismic wave speed changes may not be adequately captured by linear elastic or visco-elastic models (Johnson and Sutin, 2005; Rivière et al., 2015; Manogharan et al., 2022), indicating the need for more advanced physics-based frameworks.

The nonlinear mechanical responses become most prominent when seismic waves propagate through soft sediments, typically located a few hundred meters below the ground surface (Wang et al., 2021). Soft sediments typically exhibit low seismic wave speeds, amplifying the strain field to values exceeding 10^{-3} and reducing the shear modulus by more than 50% (Roten et al., 2012; van Ginkel et al., 2022). This behavior is accompanied by the damping of ground motion amplitudes (Rajaure et al., 2017) and a change in the frequency components of seismograms toward lower values (Bonilla et al., 2011; Castro-Cruz et al., 2020). Accounting for such nonlinear mechanical responses is crucial for modeling ground motions at both low frequencies ($\leq$1 Hz, Roten et al., 2014) and high frequencies (Roten et al., 2016).

Capturing co-seismic wave speed changes relies on adequate nonlinear rock models. Some of such nonlinear models originate from thermodynamic processes at the microscopic scale (Iwan, 1967; Delsanto and Scalerandi, 2003; Lebedev and Ostrovsky, 2014). These models usually introduce more parameters than those constrained by observations (Wang et al., 2021). As a practical compromise, continuum damage mechanics (CDM) models are based on simplified assumptions about microscopic material deficiencies and describe macroscopic stress-strain relationships using fewer parameters (Kachanov, 1986; Desmorat, 2016; Gabriel et al., 2021). Within this framework, the CDM model by Lyakhovsky et al. (1997a) and the internal variable model (IVM) by (Berjamin et al., 2017) have been shown to reproduce laboratory measurements of co-seismic wave speed changes in rocks (Renaud et al., 2012; Feng et al., 2018; Manogharan et al., 2022; Niu et al., 2024). For unconsolidated sediments, such as soil, the loss of stiffness under cyclic loading is effectively described by a hyperbolic shear modulus reduction curve (Kramer and Stewart, 2024; Vardanega and Bolton, 2013).

Previous studies have developed numerical methods for modeling co-seismic wave speed changes in 1D (Remillieux et al., 2017; Berjamin et al., 2017) and 2D (Berjamin et al., 2019; Niu et al., 2024), which have been validated through laboratory experiments. The fourth-order staggered-grid finite difference method, implemented in the software AWP-ODC, resolves shear modulus reduction using the IWAN model (Iwan, 1967) in 3D, with a focus on capturing nonlinear effects in soft sediments for ground motion simulations (Cui et al., 2010; Roten et al., 2023). Consolidated rocks, such as granite, also experience co-seismic wave speed reductions (Shokouhi et al., 2017), which remain mostly smaller than 1%. Resolving such small changes is computationally expensive using the IWAN model (Roten et al., 2023). Leveraging this phenomenon as a probe for rock types and subsurface physical conditions (Rivière et al., 2015; Manogharan et al., 2022) requires the development of a numerical framework capable of resolving 3D co-seismic wave speed changes in consolidated rocks. Such a framework would act as a critical bridge, enabling realistic regional-scale modeling of co-seismic wave speed changes directly informed by laboratory data. However, to the best of the authors' knowledge, this approach remains unrealized to date.

To fill this gap, we here propose and validate a novel algorithm based on the discontinuous Galerkin method (Cockburn and Shu, 1989; Dumbser and Käser, 2006; Dumbser et al., 2008) for modeling seismic wave propagation in 3D nonlinear rock rheologies. We implement this algorithm in the open-source software SeisSol (Heinecke et al., 2014a; Uphoff et al., 2017; Krenz et al., 2021; Uphoff et al., 2024), which is specifically suited for field-scale seismic wave propagation simulations involving heterogeneous velocity models and complex geometries. We verify the implementation by comparison against analytical solutions and present scaling tests on the Frontera supercomputer (Stanzione et al., 2020).

Using this framework, we simulate co-seismic wave speed changes and ground motions during the 2015 M_W 7.8 Gorkha earthquake in the Kathmandu Valley. This earthquake occurred directly beneath the Kathmandu Valley (Fan and Shearer, 2015), causing over 9,000 fatalities, extensive property damage, and significant loss of life in Nepal. Ground motion records reveal that the Kathmandu basin experienced unexpectedly weak high-frequency motions but larger low-frequency motions compared to empirical predictions (Takai et al., 2016). This behavior has been attributed to nonlinear site response (Castro-Cruz et al., 2020). To evaluate this hypothesis, we utilize an experimentally constrained nonlinear model, IVM, to simulate the co-seismic wave speed changes in rocks (Niu et al., 2024). We also adapt IVM such that it captures the hyperbolic shear modulus reduction curve in soft sediments. By integrating laboratory data, our simulation results quantify the spatial variability of field-scale co-seismic wave speed changes and their impact on peak ground motions, offering important insights for seismic hazard assessment.

2 Methods

When nonlinear rock rheology is incorporated into seismic wave propagation simulations, the governing wave equations are classified as nonlinear hyperbolic partial differential equations (PDE, Lax, 2005). A key characteristic of these equations is their potential for solutions to develop spatial discontinuities, even if the initial conditions are smooth (LeVeque, 2002). Solving these equations requires an algorithm that can adequately resolve discontinuities while maintaining numerical stability. Additionally, to allow realistic large-scale earthquake simulations and energy efficiency, the implementation must scale efficiently across a large number of compute ranks (Carrington et al., 2008; Cui et al., 2010; Heinecke et al., 2014b; Ilsche et al., 2019; Uphoff, 2020; Krenz et al., 2021).

This section describes how we formulate the two nonlinear damage rock models employed in this work as a system of nonlinear hyperbolic PDEs. We then outline the spatial and temporal discretization of these PDEs using the discontinuous Galerkin method (Hesthaven and Warburton, 2007; Cockburn et al., 2012).

2.1 Mathematical framework for nonlinear wave propagation in damaged rocks

To model co-seismic wave speed changes and their impact on ground motions, we adopt the recent mathematical framework by Niu et al. (2024) that utilizes a continuum damage model (CDM, Lyakhovsky et al., 1997a) and an internal variable model (IVM, Berjamin et al., 2017). Both models have been shown to quantitatively match laboratory data (Manogharan et al., 2022; Feng et al., 2018; Niu et al., 2024). 2D solutions for co-seismic wave speed changes modeled with the IVM implemented in the DG method have been validated against the results of the finite volume method (Niu et al., 2024).

In the following, we present a unified DG algorithm for nonlinear wave propagation, designed to accommodate any nonlinear rock model explicitly formulated as a system of hyperbolic equations, including IVM and CDM. This approach extends our previous 2D implementation of IVM to 3D and applies our 3D discontinuous Galerkin (DG) method to model wave propagation using the CDM nonlinear rock model.

Hyperbolic PDEs are required for implementation in SeisSol (Uphoff et al., 2024). Previous work implemented linear visco-elasticity (Käser et al., 2007; Uphoff, 2020) and Drucker-Prager elasto-plasticity (Wollherr et al., 2018) using the DG algorithm for linear hyperbolic equations. In contrast, CDM and IVM introduce nonlinear hyperbolic PDEs, which we summarize as follows:

$$\begin{cases} \dfrac{\partial \varepsilon_{ij}}{\partial t} & = \dfrac{1}{2}\left(\dfrac{\partial v_i}{\partial x_j} + \dfrac{\partial v_j}{\partial x_i}\right) \\ \rho \dfrac{\partial v_i}{\partial t} & = \dfrac{\partial \sigma_{ij}(\underline{\underline{\varepsilon}}, \alpha)}{\partial x_j} \\ \dfrac{\partial \alpha}{\partial t} & = r_\alpha(\underline{\underline{\varepsilon}}, \alpha) \end{cases}, \tag{1}$$

where $\underline{\underline{\varepsilon}} = \varepsilon_{ij}$ and σ_{ij} denote, respectively, the total strain and stress tensors, v_i is the vector for particle velocity, and ρ is the material mass density. α is a damage variable, which is 0 for intact rock and 1 for fully damaged rock. r_α defines the evolution rate of the damage variable α as a function of the strain tensor and the damage variable itself.

IVM and CDM are both extensions of the classical linear elastic stress-strain relationship that is parameterized with two Lamé parameters, i.e., λ_0 and μ_0 (Landau et al., 1986). The differences between the two models lie in how they are extended to include nonlinear functions of the stress tensor $\sigma_{ij}(\underline{\underline{\varepsilon}}, \alpha)$, and how the source term $r_\alpha(\underline{\underline{\varepsilon}}, \alpha)$ is defined.

For the IVM (Berjamin et al., 2017), we write

$$\begin{cases} \sigma_{ij}(\underline{\underline{\varepsilon}}, \alpha) = (1-\alpha)(\lambda_0 I_1 \delta_{ij} + 2\mu_0 \varepsilon_{ij} + \sigma_{ij}^{\mathrm{mur}}) \\ r_\alpha(\underline{\underline{\varepsilon}}, \alpha) = \dfrac{1}{\gamma_b \tau_b}[\dfrac{1}{2}\lambda_0 I_1^2 + \mu_0 I_2 + W^{\mathrm{mur}} - \phi(\alpha)] \end{cases}, \tag{2}$$

where $\phi(\alpha) = \gamma_b[\alpha/(1-\alpha)]^2$ is the storage energy, γ_b is the scale of $\phi(\alpha)$ with units in pascals (Pa), and τ_b is the time scale of damage evolution. $I_1 = \varepsilon_{kk}$ and $I_2 = \varepsilon_{ij}\varepsilon_{ij}$ are two strain invariants.

The original IVM framework can incorporate the classical Murnaghan nonlinear elasticity (Murnaghan, 1937) with three additional material parameters l_0, m_0, and n_0 to account for third-order terms in the non-quadratic components of the elastic energy function $W^{\mathrm{mur}} = (l-m)/3I_1^3 + mI_1I_2 + nI_3$, where $I_3 = \delta_{ijk}\varepsilon_{i1}\varepsilon_{j2}\varepsilon_{k3}$. This leads to the additional stress component $\sigma_{ij}^{\mathrm{mur}} = a_0\delta_{ij} + a_1\varepsilon_{ij} + a_2\varepsilon_{ik}\varepsilon_{kj}$, where the coefficients $a_0 = l_0 I_1^2 - (m_0 - 1/2n_0)(I_1^2 - I_2)$, $a_1 = (2m_0 - n_0)I_1$, and $a_2 = n$. δ_{ijk} denotes the Levi-Civita permutation symbol.

While Murnaghan nonlinear elasticity is useful for modeling some instances of stress-induced anisotropy (Sharma, 2010), it may not adequately explain the observed co-seismic wave speed reductions under dynamic stress fields (Gassenmeier et al., 2016; Berjamin et al., 2017; Niu et al., 2024). Therefore, in the following, we choose to set $l_0 = m_0 = n_0 = 0$ to exclude the additional terms of Murnaghan nonlinear elasticity in our proposed algorithm. This also ensures that $\sigma_{ij}^{\mathrm{mur}} = W^{\mathrm{mur}} = 0$ in Eq. (2). However, in Sections 3.1 and 3.2, we demonstrate that our proposed algorithm remains generic and can accurately resolve nonlinear effects resulting from a simplified Murnaghan nonlinear elasticity in 1D.

For the CDM (Lyakhovsky et al., 1997a, 2016), we write

$$\begin{cases} \sigma_{ij}(\underline{\underline{\varepsilon}}, \alpha) = \lambda_0 I_1 \delta_{ij} - \alpha\gamma_r\sqrt{I_2}\delta_{ij} + [2(\mu_0 + \alpha\xi_0\gamma_r) - \alpha\gamma_r\xi]\varepsilon_{ij} \\ r_\alpha(\underline{\underline{\varepsilon}}, \alpha) = \begin{cases} C_d\gamma_r I_2(\xi - \xi_0) & \text{, if } \xi - \xi_0 > 0 \\ 0 & \text{, if } \xi - \xi_0 \leq 0 \end{cases} \end{cases}, \tag{3}$$

where γ_r is a third modulus originating from the homogenization of parallel cracks (Lyakhovsky et al., 1997b), and C_d is a damage evolution coefficient. $\xi = I_1/\sqrt{I_2}$ is derived from the two strain invariants. It grows from $-\sqrt{3}$ for isotropic compression to $\sqrt{3}$ for isotropic extension. The damage α starts to accumulate as the strain state deviates farther enough from the isotropic compression. This is expressed as $\xi - \xi_0 > 0$, where ξ_0 is a material parameter that is usually negative for rocks (Lyakhovsky et al., 2016).

In this work, we propose a generic algorithm that can be used for either IVM or CDM. Both models can generally be formulated as a nonlinear hyperbolic system of conservation laws with an additional source term following Dumbser et al. (2008):

$$\frac{\partial u_p}{\partial t} + \frac{\partial F_p^d(\underline{v}, \underline{\underline{\varepsilon}}, \alpha)}{\partial x_d} = s_p(\underline{v}, \underline{\underline{\varepsilon}}, \alpha), \tag{4}$$

where $u_p = (\varepsilon_{xx}, \varepsilon_{yy}, \varepsilon_{zz}, \varepsilon_{xy}, \varepsilon_{yz}, \varepsilon_{zx}, v_x, v_y, v_z, \alpha)^T$ is a vector of the conservative variables. ε_{xx}, ε_{yy}, ε_{zz}, ε_{xy}, ε_{yz}, and ε_{zx} are six components of the strain tensor $\underline{\underline{\varepsilon}} = \varepsilon_{ij}$; v_x, v_y and v_z are the three components of the particle velocity vector $\underline{v}$. The flux term F_p^d represents the rates at which the conservative variable u_p gets transferred through a unit area in the direction x_d (LeVeque, 2002). The source vector $s_p = (0, 0, 0, 0, 0, 0, 0, 0, 0, r_\alpha)^T$ with only one non-zero element r_α defined in Eq. (2) for IVM or Eq. (3) for CDM.

2.2 Numerical discretization of the nonlinear wave equations

Our implementation adopts the Arbitrary-accuracy DERivative (ADER) discretization in time (Titarev and Toro, 2002; Dumbser et al., 2008; Gassner et al., 2011), and the discontinuous Galerkin (DG) discretization in space (Cockburn and Shu, 1989; Dumbser et al., 2008). Here, we apply a linearization to the nonlinear hyperbolic PDEs to simplify the adaptation of the algorithm to both damage models, as outlined in Section 2.1. This linearization also minimizes the necessary changes to the existing data structure in SeisSol (Uphoff, 2020; Uphoff et al., 2024). We provide a detailed description of the method in this section and Appendix A and will demonstrate in Section 3.1 that the algorithm still converges using linearization.

We subdivide the computational domain into tetrahedral elements. Within each element $\mathcal{T}_m$, we use a modal discontinuous Galerkin approach to approximate the conservative variables as $\underline{u} \approx \underline{u}^h$, employing Dubiner's orthogonal polynomial basis functions, $\phi_l(\underline{x})$ (Cockburn et al., 2012). The temporal evolution of the solution is captured using time-dependent coefficients $Q_{lp}(t)$ defined as:

$$u_k^h(\underset{\sim}{x}, t) = \sum_{l=1}^{L} U_{lk}(t)\phi_l(\underset{\sim}{x}),\ k = 1,\ 2,\ ...,\ K, \tag{5}$$

where the index l runs from 1 to $L = (p+1)(p+2)(p+3)/6$ for a polynomial degree p. The index k runs from 1 to K, the number of elements in the conservative variables u_p in Eq. (4). We discretize the time-dependent coefficients using the ADER scheme with a Taylor series as

$$U_{lp}(t) = \sum_{i=0}^{N} \frac{(t-t_n)^i}{i!}\mathcal{D}_{lp}^i, \tag{6}$$

where $\mathcal{D}_{lp}^0 = U_{lp}(t_n)$, and $\mathcal{D}_{lp}^i = \left.\frac{\partial^i U_{lp}}{\partial t^i}\right|_{t=t_n}$ for $i \geq 1$.

This discretized system is solved in two steps. First, we linearize the nonlinear hyperbolic system and estimate $\mathcal{D}_{lp}^i$ using the Cauchy-Kovalevskaya approach (Kovalevskaja, 1874). In the following, we refer to this step as the "prediction step". It allows us to obtain the estimated $U_{lp}(t)$ within one stage, as opposed to the Runge-Kutta method (Butcher, 2007; Gassner et al., 2011). In the second step, we use the predicted $U_{lp}(t)$ to integrate the conservative variables over time while adequately addressing spatial discontinuities at element interfaces, which we refer to as the "correction step". In Appendix A, we detail the algorithm to solve these discretized nonlinear wave equations proposed in this work, including how we implement free-surface and absorbing boundary conditions.

3 Verification against analytical solutions

In this section, we verify the proposed numerical algorithm by solving three problems with known analytical solutions. It is essential to confirm that the proposed numerical scheme converges to the correct solutions before applying it to large-scale seismological applications, for which it is impossible to derive analytical solutions for nonlinear wave equations in 3D.

We first compare our numerical solutions for plane waves in 3D with two existing analytical solutions in 1D: (1) the nonlinear Riemann problem and (2) the generation of high-frequency harmonics from a single-frequency source. For 3D analysis, we show that the proposed algorithm can accurately resolve stress-induced anisotropy of CDM, in agreement with the analytical solutions from Hamiel et al. (2009).

3.1 The nonlinear 1D Riemann problem

The Riemann problem is a canonical benchmark with analytical solutions for nonlinear hyperbolic PDEs in one dimension (LeVeque, 2002). It is defined by initial conditions with a single discontinuous interface, where the variables have one set of uniform values on one side of the interface while having another set of different uniform values on the other side. The Riemann problem is widely used to assess whether numerical algorithms can accurately resolve discontinuities in solutions, which is an important feature of nonlinear hyperbolic PDEs.

We use a plane shear wave in 3D to configure the 1D Riemann problem. The plane shear wave comprises ε_{xy} and v_y. We set the remaining components to zero. We define the wavefront as parallel to the $y-z$ plane, such that the domain only varies in the x direction, which simplifies Eqs. (1) to:

$$\begin{cases} \dfrac{\partial \varepsilon_{xy}}{\partial t} & = \dfrac{1}{2}(\dfrac{\partial v_y}{\partial x}) \\ \rho \dfrac{\partial v_y}{\partial t} & = \dfrac{\partial \sigma_{xy}(\varepsilon_{xy})}{\partial x} \end{cases}, \tag{7}$$

where we define $\sigma_{xy} = 2\mu(1-\beta\varepsilon_{xy})\varepsilon_{xy}$ as a nonlinear function of ε_{xy} with β being the first order nonlinear coefficient (Landau et al., 1986).

This formulation is comparable to a 1D reduction of Murnaghan nonlinear elasticity, as described after Eq. (2). Meurer et al. (2002) provide analytical solutions to the Riemann problem for Eqs. (7), incorporating the simplified 1D nonlinear stress-strain relationship.

We choose material parameters and initial conditions to show the accuracy of our proposed algorithm for materials with strong nonlinearity. Therefore, we set the following initial conditions for the Riemann problem.

$$[\varepsilon_{xy}, v_y]^T = \begin{cases} [0.1, -0.5]^T \text{ for } x < 0 \\ [0.2, -1.0]^T \text{ for } x \geq 0 \end{cases}. \tag{8}$$

These initial conditions are also shown as dashed curves in Fig. 1. We set $\rho = 1.0$, $\mu = 1.0$ and $\beta = 10.0$. The black curves shown in Fig. 1 are the corresponding analytical solutions evaluated after 4 ms. The solutions feature one shock wave (interface with sharp discontinuities, marked with red dashed rectangles) and one rarefaction wave (a smooth transition from one state on the left to another state on the right, highlighted by purple rectangles).

We compare this analytical solution to several numerical results obtained with a polynomial order $p = 3$ on three mesh sizes: $h = 2.5$ mm (dashed blue curves), $h = 0.5$ mm (dash-dotted blue curves) and $h = 0.1$ mm (solid blue curves). Figs. 1c and 1d focus on the numerical solutions at the shock wavefront and at the rarefaction wavefront. The shock wave exhibits stronger spatial oscillations than the rarefaction wave, primarily due to solution variations within each element. The amplitude and wavelength of these oscillations both decrease as the mesh is refined, indicating that oscillations can be effectively suppressed with mesh refinement.

We analyze the convergence rates for different orders of polynomial basis functions and present the results in Fig. 1b. We quantify the L_2 errors in our numerical simulations at $t = 4$ ms using the L_2 norms of the differences between the analytical solution u^{ana} and the numerical solutions u^{num}. We determine the convergence rate by analyzing the reduction of L_2 errors with mesh size h on a logarithmic scale. The observed convergence rate remains first order across all polynomial degrees tested (1 to 5), indicating that this algorithm does not achieve arbitrarily high-order accuracy at discontinuities. Nonetheless, we still observe lower L_2 errors with higher-order basis functions on the same mesh (p-convergence, Wollherr et al., 2018). We will discuss the underlying causes and potential improvements in Section 5.1.

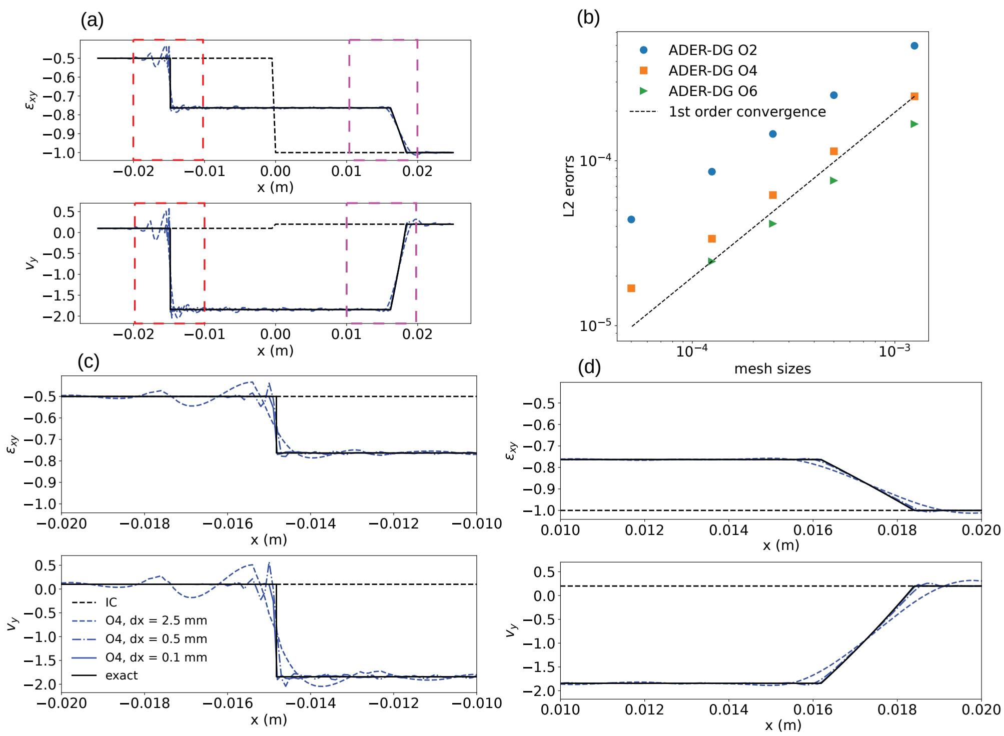

Figure 1. Comparison of the analytical and the numerical solutions with varying mesh resolution h and polynomial degrees p for the Riemann problem. (a) Comparison of numerical and analytical solutions of v_y and ε_{xy} using shape functions of polynomial degree 3 (O4, representing convergence rate of order 4). We show solutions for three mesh sizes: $h = 2.5$ mm (dashed blue curves), $h = 0.5$ mm (dash-dotted blue curves) and $h = 0.1$ mm (solid blue curves). The initial conditions (IC) are illustrated as dashed black curves, and the analytical solutions are given in solid black curves. (b) Convergence analysis showing the error decay with decreasing mesh size h, for simulations using basis functions of polynomial degrees 1 (O2, blue dots), 3 (O4, orange rectangles), and 5 (O6, green triangles). The dashed black line indicates first-order convergence as a reference. Panels (c) and (d) highlight specific features of (a): the shock wavefront (inside the dashed red rectangles) in (c) and the rarefaction wavefront (inside the dashed pink rectangles) in (d).

3.2 1D frequency modulation by nonlinear materials

The generation of harmonics from a single-frequency source is a mathematically intriguing problem in nonlinear wave propagation. It is widely used to quantify material nonlinearity in acoustic testing and non-destructive evaluation (Shah and Ribakov, 2009; Matlack et al., 2015; Jiao et al., 2025). This behavior is a distinctive and general feature of wave propagation in nonlinear materials, existing in both the Murnaghan nonlinear elasticity and the nonlinear stress-strain relationship in Eq. (3) of CDM.

For the 1D Murnaghan nonlinear elasticity defined in Eq. (7), we use the 1D analytical asymptotic solutions from McCall (1994) derived using perturbation theory, which describes how the amplitudes of generated harmonics depend on the nonlinear parameters of the material, the propagation distance, and the source amplitude. We use this analytical reference solution in the following to show that our proposed algorithm can accurately resolve the generation of harmonics in 1D nonlinear numerical simulations, exemplarily for 1D Murnaghan nonlinear elasticity.

We adopt the same plane shear wave description as in Section 3.1 for the single-frequency source setup and solve the same nonlinear wave equations as in Eqs. (7). The simulation is carried out in a cubic domain [-0.025, 0.025] m × [-0.025, 0.025] m × [-0.025, 0.025] m, with periodic boundary conditions on all faces. We define the initial conditions for the plane wave such that the wavelength is 0.05 m, matching the length of the simulation domain:

$$[\varepsilon_{xy}, v_y]^T = [V_0/c_s, V_0]^T \times \sin(2\pi kx), \tag{9}$$

where $k = 20\ \mathrm{m}^{-1}$ and $c_s = \sqrt{\mu/\rho}$ is the shear wave speed. We set $\mu = 82.7$ GPa, $\rho = 2473\ \mathrm{kg/m}^3$, and vary the wave amplitude V_0 and the nonlinear coefficient β to assess whether the simulation results can quantitatively match the analytical asymptotic solutions at a small propagation distance in Eq. (34) of McCall (1994). We note that the shear modulus defined here is unrealistically high for rocks; however, these parameters are chosen solely to verify that the numerical solutions are mathematically consistent with the asymptotic solutions. Additionally, the asymptotic solution from McCall (1994) indicates that the amplitude of the second-order harmonics does not depend on μ.

The single-frequency waveform is modulated by the nonlinear parameter β during propagation. Fig. 2a shows the modeled time series at distances of 0.0, 0.5, and 1.0 m from the source. While the peak amplitude and period remain unchanged, the shape of the waveform changes within one period due to the high-order harmonic generation.

We show the generated harmonics 1.0 m away from the source in Fig. 2b. McCall (1994) derived an asymptotic solution for the amplitude of the second-order harmonics at small distances away from the source. This analytical asymptotic solution is no longer valid at larger distances. As shown in Fig. 2c, these analytical solutions (dashed curves) serve as exact asymptotes to the numerical solutions (solid curves) at small distances. We present results for three sets of parameters, demonstrating the robustness of the match between the analytical asymptotic and our numerical solutions.

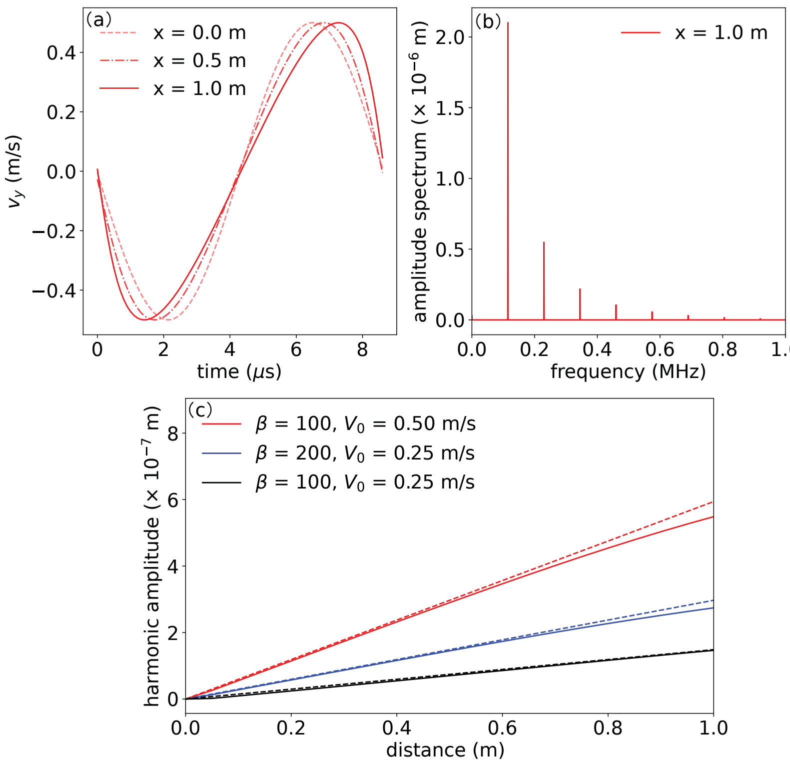

Figure 2. Comparison between numerical and analytical asymptotic solutions for wave propagation from a single-frequency source. (a) Recorded time series of v_y at the source (dashed red curve) and at distances of 0.5 m (dash-dotted red curve) and 1.0 m (solid red curve) from the source. (b) The frequency amplitude spectrum of the time series of v_y at 1.0 m from the source shows the generation of high-order harmonics, which are multiples of the fundamental frequency. (c) Comparison between the analytical asymptotic solutions (dashed curve) and the numerical (solid curves) solutions. We show three sets of parameters, with variations in the nonlinear modulus β and the amplitude of the source V_0. We note that the analytical asymptotic solutions are known to be only valid at short distances from the source.

3.3 3D stress- and damage-induced anisotropy

Rocks exhibit various types and levels of anisotropy (Nur and Simmons, 1969; Nur, 1971; Browning et al., 2017). This anisotropy arises from various internal flaws, such as cracks, joints, and fabric development due to differential stress and strain during tectonic processes (Panteleev et al., 2024). The anisotropy of seismic wave propagation in such rocks can depend on the stress state and accumulated damage, a phenomenon referred to as stress- and damage-induced anisotropy. This dependence leads to nonlinear stress-strain relationships, which are important for capturing path and site effects in earthquake simulations. Accurately resolving these effects is essential to advance numerical simulations of ground motions.

Both Murnaghan nonlinear elasticity and CDM describe stress-induced anisotropy (Johnson and Rasolofosaon, 1993; Hamiel et al., 2009). However, while Murnaghan nonlinear elasticity may require unrealistically high values for l_0, m_0, and n_0 in Eq. (2), CDM provides a physical framework that can describe stress- and damage-induced anisotropy and has been experimentally validated (Hamiel et al., 2009). Here, we demonstrate that our proposed generic algorithm is suitable for implementing CDM by verifying its ability to resolve stress- and damage-induced anisotropy in 3D. We compare the numerical results with the analytical solutions derived by Hamiel et al. (2009).

We set up several plane-wave initial value problems to investigate how the P, S, and qS wave speeds depend on the orientation of the initial stress with respect to the normal vector of the initial wavefront and the damage level α. The qS wave speed is the additional wave speed resulting from anisotropy (Harris et al., 2009). Without loss of generality, we fix the normal vector of the wavefront to (1,0,0) and vary only the initial stress field and α. Since CDM represents the seismic wave field using the total strain tensor $\underline{\underline{\varepsilon}} = \underline{\underline{\varepsilon}}^{\text{pre}} + \underline{\underline{\varepsilon}}^{\text{dyn}}$, we pragmatically apply initial stress by prescribing initial strain values.

The initial strain field consists of two parts: (i) a uniform strain field $\underline{\underline{\varepsilon}}^{\text{pre}}$, that represents the stress (strain) state of the rocks before dynamic perturbations from seismic waves; and (ii) the perturbation field $u_i^{\text{dyn}} = (\varepsilon_{xx}^{\text{dyn}}, \varepsilon_{yy}^{\text{dyn}}, \varepsilon_{zz}^{\text{dyn}}, \varepsilon_{xy}^{\text{dyn}}, \varepsilon_{yz}^{\text{dyn}}, \varepsilon_{zx}^{\text{dyn}}, v_x, v_y, v_z, \alpha)^T$, substituted into Eq. (4). The expression for u_i^{dyn} depends on the wave type and is given as

$$\begin{cases} u_i^{\text{dyn}} = A_0 r_i^1 \sin(2\pi k x) & \text{, for P wave} \\ u_i^{\text{dyn}} = A_0 r_i^2 \sin(2\pi k x) & \text{, for S or qS wave ,} \\ u_i^{\text{dyn}} = A_0 r_i^3 \sin(2\pi k x) & \text{, for S or qS wave} \end{cases} \tag{10}$$

where the three vectors r_i^1, r_i^2 and r_i^3 are defined in Eq. (A21). The classification of r_i^2 or r_i^3 is either S or qS waves depending on the orientation of the uniform strain field $\underline{\underline{\varepsilon}}^{\text{pre}}$.

We list the material properties of the CDM model and the initial values of the PDEs in Table 1. The corresponding mathematical formulation is provided in Eq. (3). We adopt the same cubic geometry as in Section 3.2.

We set the initial damage variable α to 0.5. We define $\underline{\underline{\varepsilon}}^{\text{pre}}$ in its principal coordinate system as $(\varepsilon_{xx}^{\text{pre}}, \varepsilon_{yy}^{\text{pre}}, \varepsilon_{zz}^{\text{pre}}, \varepsilon_{xy}^{\text{pre}}, \varepsilon_{yz}^{\text{pre}}, \varepsilon_{zx}^{\text{pre}})^T = (1 \times 10^{-3}, 0, 0, 0, 0, 0)^T$. Following Hamiel et al. (2009), we initially align the global coordinate system in the numerical simulation with the principal coordinate system of $\underline{\underline{\varepsilon}}^{\text{pre}}$. We then rotate $\underline{\underline{\varepsilon}}^{\text{pre}}$ counterclockwise around the z-axis by an angle ϕ^{ani}, which ranges from 0 to 180 degrees.

Figs. 3a and 3b compare analytical and numerical solutions for P waves and for S and qS waves, respectively.

Table 1. Summary of the perturbation field and the model parameters of the continuum damage model.

	Parameters	Values	Units	Parameters	Values	Units
perturbations	A_0	2.5×10^{-6}	1	k	20	m^{-1}
model para.	λ_0	32	GPa	γ_r	37	GPa
	μ_0	32	GPa	ξ_0	-0.75	1
	ρ	2760	kg/m^3	C_d	0.0	$(Pa{\cdot}s)^{-1}$

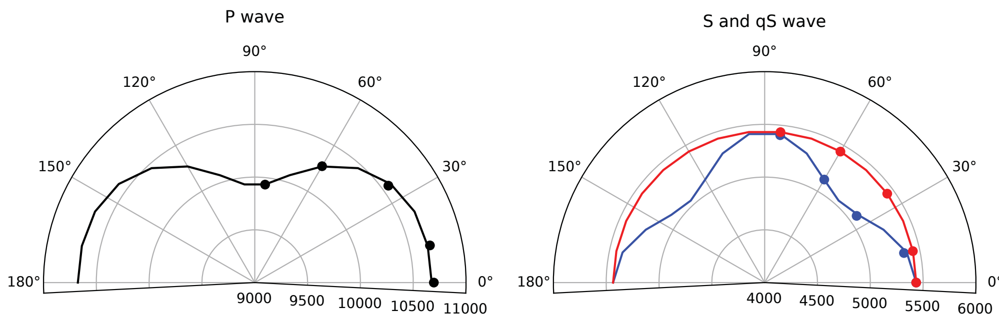

Figure 3. Comparison between analytical and numerical wave speeds of different phases for damage- and stress-induced anisotropy. (a) P-wave speed comparison, where black dots represent numerical simulation results and the black curve corresponds to the analytical solution. (b) S-wave (red curve and dots) and qS-wave (blue curve and dots) comparisons, showing numerical results alongside analytical predictions.

4 Modeling co-seismic wave speed changes during the 2015 Gorkha earthquake

We apply our verified numerical framework to model co-seismic wave speed changes during the April 25, 2015, M_w 7.8 Gorkha earthquake in the Kathmandu Valley. We set up a geometrically complex 3D simulation of nonlinear seismic wave propagation from a finite source model of the 2015 M_w 7.8 Gorkha earthquake. Our setup captures key features relevant for modeling earthquake-related ground motions: a geometrically complex low-velocity sedimentary basin, layered subsurface geometry that represents different geological units, and a finite source model accounting for the directivity effect of a large earthquake.

4.1 Numerical setup, nonlinear parameters and source model

As shown in Fig. 4b, the 3D computational domain has a size of $440\times380\times200$ km^3. The velocity model includes five geological units (Table 2). The first unit accounts for the surface topography and bathymetry of the shallow sediments within the Kathmandu basin with a low S-wave velocity of 200 m/s (Bohara and Ghimire, 2015). The second unit captures the strong topographical variation outside of the sedimentary basin within the Kathmandu Valley. We sample the surface topography with a resolution of 5 km. Units 3 through 5 are derived from a regional 1D velocity model (McNamara et al., 2017).

We will compare the effects of three inelastic rheologies and elastic behavior using otherwise the same model setup: (i) visco-elastic, (ii) elasto-plastic, and (iii) internal variable model (IVM). In the visco-elastic case, we adopt the Zener model (Carcione et al., 1988) to describe viscous attenuation in SeisSol (Uphoff and Bader, 2016; Uphoff et al., 2024). We list the visco-elastic quality factors for the P-wave (Q_P) and the S-wave (Q_S) inside each layer in Table 2. The effective quality factors approximate the target quality factors well within the frequency range of 0.03 to 3 Hz. They increase asymptotically to infinity outside this frequency range, yielding close to linear elastic behavior. We set the quality factors as $Q_P = 0.1V_S$ and $Q_S = 0.05V_S$ for V_S measured in m/s following Olsen et al. (2003). In the elasto-plastic setup, the inelastic behavior is only effective inside the sedimentary basin (unit 1). We adopt the Drucker-Prager plasticity (Wollherr et al., 2018) and provide the material parameters in the footnote of Table 2.

We employ the IVM (Berjamin et al., 2017) to investigate nonlinear co-seismic wave speed changes outside the fault core and extending over 100 kilometers from the fault. The model has been validated in Niu et al. (2024) against two sets of laboratory experiments, which demonstrates its ability to quantify nonlinear co-seismic wave speed changes in granite samples (Manogharan et al., 2022) and sandstone samples (Feng et al., 2018). The mathematical description of IVM nonlinearity is summarized in Eq. (2). We refer to Berjamin et al. (2017) and Niu et al. (2024) for more details. The chosen model parameters of the IVM within each region are given in Table 2. The nonlinear parameters inside the sedimentary basin (unit 1) are calibrated to match the modulus reduction curve from a 2D analysis presented in Oral et al. (2022), constrained by the shift in resonance frequencies observed during significant events with magnitudes exceeding M_W 6.5 within the Kathmandu Valley (Rajaure et al., 2017). For the layered bedrocks (units 2 to 5), we constrain the nonlinear IVM parameters from experiments by Manogharan et al. (2022) investigating nonlinear co-seismic wave speed changes of Westerly granite samples. As discussed in Niu et al. (2024), the parameter γ_b, which determines the amplitude of stationary wave speed reductions under dynamic perturbations, can be constrained from experiments. However, the time scale τ_b, which governs how quickly rocks reach the stationary state, remains highly uncertain. Here, we assume $\tau_b = 10$ s in units 1 to 5, which is consistent with the time scale at which the changes in wave speed stabilize, as observed in experiments on Westerly granite samples (Manogharan et al., 2021).

Table 2. Material parameters for each geological unit of the computational domain.

region	depth	c_p	c_s	ρ	Q_p	Q_s	γ_b	τ_b
unit	km	m/s	m/s	kg/m^3	1	1	kPa	s
1*	variable	300	200	1400	20	10	0.5	10
2	variable - 3	5500	3250	2700	325	162.5	356	10
3	3 - 23	5502	3600	2700	360	180	437	10
4	23 - 45	6100	3600	2900	360	180	437	10
5	45 - 200	8100	4500	3300	450	225	550	10

* Plasticity is only effective inside the sedimentary basin in the elasto-plastic simulation. The yielding strength is 224 kPa, with an internal friction angle of 26 degrees and a visco-plastic relaxation time T_v of 0.05 s (Wollherr et al., 2018).

We employ a polynomial degree of five and SeisSol's velocity-aware meshing capabilities to adapt the element size h for each of the five geological units, ensuring at least three elements per S-wave wavelength of a maximum target frequency. In this way, our simulations resolve up to 0.5 Hz of the seismic wavefield everywhere in the domain, including in the complex geometry, low-velocity basin. We refine this mesh around the finite fault plane, which is embedded in units 1 to 3, to $h = 800$ m for a higher resolution of the kinematic rupture evolution. As a result of the velocity-aware meshing, the sedimentary basin (unit 1) is resolved with a higher mesh resolution of $h \approx 133$ m. In units

2 and 3, mesh resolution gradually decreases, and h increases from 800 m near the finite fault plane to ≈2000 m away from the source region.

In this example, we implement the finite source model of Wei et al. (2018) on a meshed finite fault plane to represent the M_W 7.8 Gorkha earthquake. We do not model the spontaneous dynamic rupture process on the fault. The relatively coarse kinematic source model is interpolated using 2D polynomial functions of degree three over a 186 km × 121 km rectangular fault plane, which results in 22,506 square sub-faults of size 1 km × 1 km. We infer a variable slip rate on each of these sub-faults from the finite source model. Next, we interpolate the imposed slip rates onto SeisSol's triangular fault mesh as an internal boundary condition. This implementation is based on the approach by Tinti et al. (2005); Causse et al. (2014). We use a Gaussian source time function to describe the slip rate function on each fault element (Bouchon, 1997).

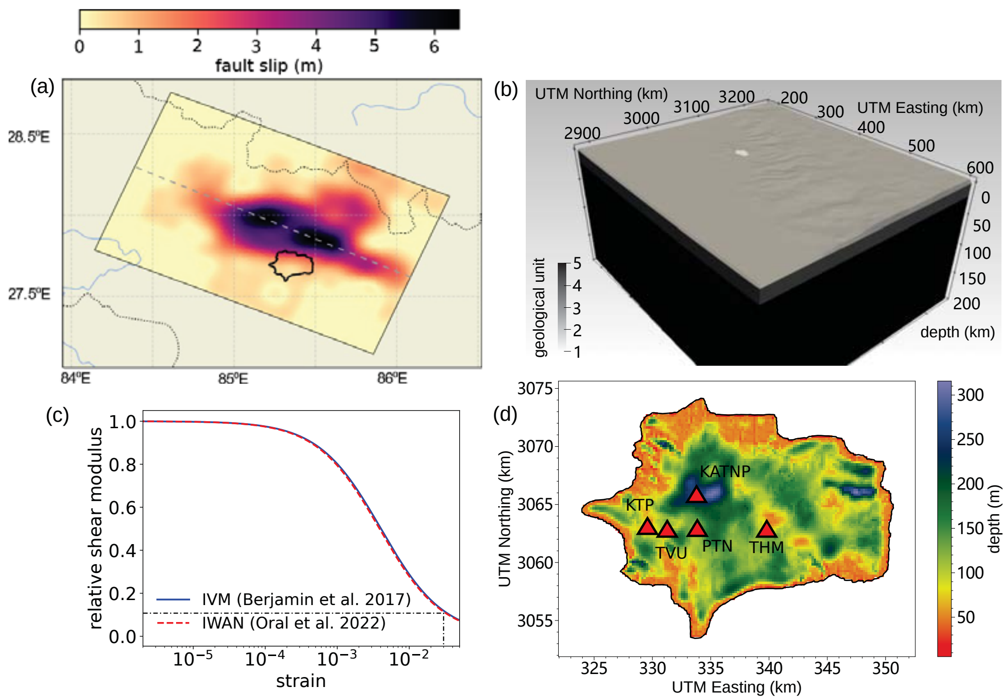

Figure 4. Model setup for the non-linear kinematic simulation of the 2015, M_W 7.8 Gorkha earthquake. (a) Fault slip distribution interpolated from Wei et al. (2018)'s kinematic source model. The dashed gray line indicates the 12-km depth slice shown in Fig. 5a. (b) Computational domain, consisting of five geological units. We incorporate topography, as well as the bathymetry of the sedimentary basin (white region at the upper boundary of the domain). (c) Shear modulus reduction with strain amplitude of the IVM model (blue curve) within the basin that has been parameterized to match the IWAN model (dashed red curve, Iwan, 1967). (d) Map view of sedimentary basin depth variation, with five strong motion stations (Takai et al., 2016) marked by red triangles.

4.2 Large-scale nonlinear co-seismic wave speed changes

Our nonlinear simulations reveal a significant reduction of co-seismic wave speed changes following the Gorkha earthquake across a vast region (Fig. 5). Fig. 5a shows wave speed changes 80 s after the rupture onset at 12 km depth. Nonlinear co-seismic wave speed reductions near the source range between 1% and 10% and are particularly pronounced close to the fault plane. For example, in the 12-km depth slice shown in Fig. 5a), the dashed black line marks the fault plane, which hosts a high slip at this depth.

The spatial distribution of the near-fault wave speed changes correlates with the fault slip distribution (Fig. 4a), with larger reductions in areas of large fault slip. Within the range of 70 km from the fault intersection, the wave speed reductions all exceed 0.01%. This level of damage is still measurable with coda-wave- or ambient-noise-based interferometry (e.g., Brenguier et al., 2014; Gassenmeier et al., 2016; Lu and Ben-Zion, 2022).

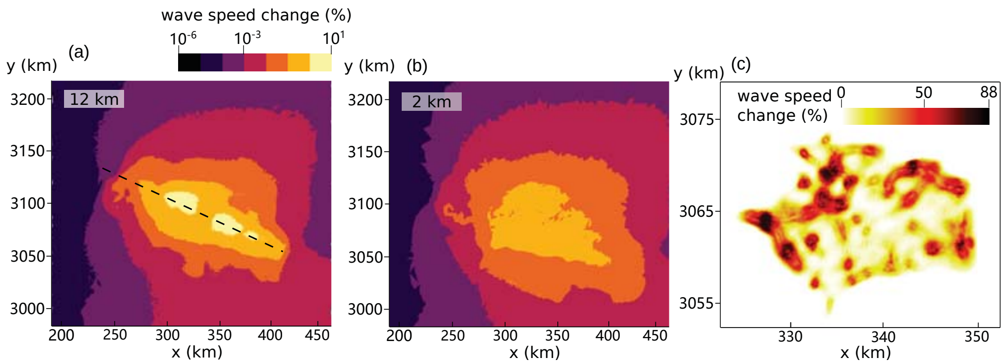

Figure 5. Map views of co-seismic wave speed changes and fault slip distribution. (a) Co-seismic wave speed changes at 12 km depth, illustrating spatial variations in velocity reduction. The dashed black line marks the fault plane location at this depth. (b) Co-seismic wave speed changes at 2 km depth, highlighting near-surface variations in wave speed reduction. (c) Co-seismic wave speed changes within the sedimentary basin, showing localized effects of nonlinearity in low-modulus materials.

We show simulated co-seismic wave speed changes at 2 km depth in Fig. 5b, which are lower compared with the changes at 12 km depth in Fig. 5a. However, the affected region is larger. At 2 km depth, wave speed reductions exceed 0.01% within a 100 km radius.

Within the sedimentary basin, nonlinear co-seismic wave speed changes are much larger (Fig. 5c), and peak changes reach 88%, corresponding to local peak strains up to 3×10^{-2} as can be seen in the shear modulus reduction curve (Fig. 4c). The spatial distribution of these changes correlates with the depth variations of the sedimentary basin (Fig. 4 d), with greater reductions in wave speed located in regions with larger basin depths. These findings align with field observations of nonlinear site effects, which report significant wave speed reductions in soft sediments during strong shaking (Bonilla et al., 2011). We will further compare the wave speed changes modeled here with observations in Section 5.

4.3 Nonlinear site effects and sedimentary basin effects

In conjunction with co-seismic wave speed changes, we observe clear effects of the nonlinear rheology on ground motions. Such effects are exemplified in synthetic seismograms comparing linear elastic, visco-elastic, perfect elasto-plastic, and nonlinear damage model simulations (Fig. 6a) at station KTP (Fig. 4d). Compared to the linear elastic case, all three other models show different levels of ground motion damping at station KTP. The nonlinear damage model exhibits the strongest wave attenuation due to progressive modulus degradation, the accumulation of damage leading to the reduction of moduli.

Our simulations suggest that co-seismic degradation of rock moduli may be an important mechanism contributing to the observed low-frequency amplification in soft sediments (Bonilla et al., 2011). We capture this effect in the spectrograms of nonlinear damage vs. linear elastic models (Figs. 6b, c). In the amplitude-frequency spectra of the modeled ground motion recorded between 20 s and 50 s after rupture onset(Fig. 6d), we observe a systematic enhancement of low-frequency components (0.1–0.2 Hz). In our simulation, this low-frequency amplification is not unique to station KTP. As shown in Fig. B1, low-frequency amplification is a general feature of the modeled ground motions at stations with high PGV values. High PGVs are correlated with significant ground deformation, leading to strong moduli reduction, consistent with the IVM shear modulus reduction curve (Fig. 4c). Such low-frequency amplification is expected during wave propagation through materials with co-propagating wave speed reduction. For example, a laboratory acoustic experiment on rock samples illustrates this phenomenon (Remillieux et al., 2017), where wave speed reduction delays the arrival time of later phases, elongating the period and consequently shifting the energy to a lower frequency.

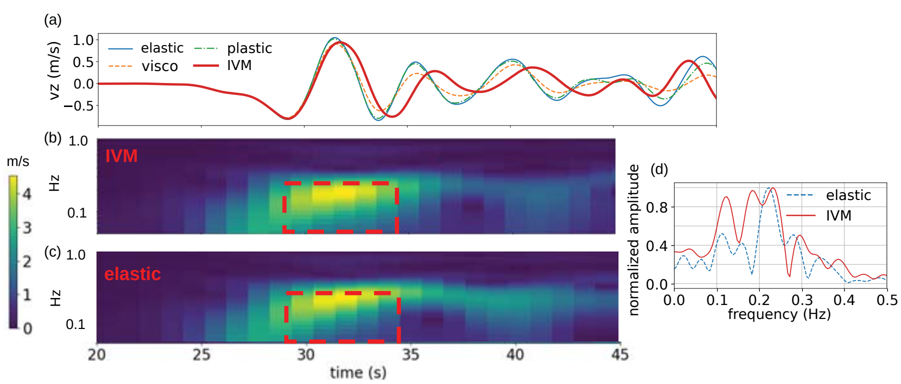

Figure 6. Time series and frequency analysis at station KTP. (a) Time series recorded at station KTP (marked in Fig. 4b) for different rheological models: elastic (solid blue curve), elasto-plastic (dash-dotted green curve), visco-elastic (dashed orange curve), and the IVM (solid red curve). (b) and (c) are spectrograms of the IVM and elastic cases, respectively, showing the frequency content of the recorded waveforms. The dashed red rectangles highlight the amplification of lower-frequency components in the IVM simulation. (d) Normalized frequency spectra of the time series recorded between 20 s and 50 s, comparing elastic (dashed blue curve) and IVM (solid red curve) models, illustrating the enhanced low-frequency content in the IVM simulation. In Fig. B1, we show the frequency spectra of time series recorded at four other stations marked in Fig. 4d.

4.4 Nonlinear rheology and ground motions (<0.5 Hz)

We compare modeled shake maps of peak ground velocity (PGV) across models with varying rheologies in Fig. 7. Linear elastic simulations show a strong correlation between the PGV in Fig. 7a and the depth of the sedimentary basin in Fig. 4d. Visco-elastic and elasto-plastic models reduce PGVs inside the Kathmandu basin, consistent with previous regional-scale studies (Narayan and Sahar, 2014; Taborda and Roten, 2015; Esmaeilzadeh et al., 2019). Extending Southern California ShakeOut simulations to include IWAN plasticity also led to a reduction in ground motion amplitudes (e.g., Roten et al., 2023).

The nonlinear damage model attenuates PGVs across both high- and low-shaking intensity regions, unlike the elasto-plastic model, which primarily reduces high PGVs (Fig. 7b). The elasto-plastic model attenuates regions of high PGVs, such as in the pink dash-dotted rectangles in Fig. 7b. However, elasto-plastic effects are negligible in regions with relatively low PGVs, such as those marked with blue dashed rectangles in Fig. 7b, which is expected from previous theoretical work and numerical simulations (e.g., Roten et al., 2014; Kojima and Takewaki, 2016; Seylabi et al., 2021). The plastic yielding surface is only reached when stress reaches a certain threshold. Below this threshold, the mechanical behavior of the material is the same as that of the linear elastic model. In contrast, the nonlinear damage model continuously degrades moduli with increasing strain amplitude (Fig. 4c).

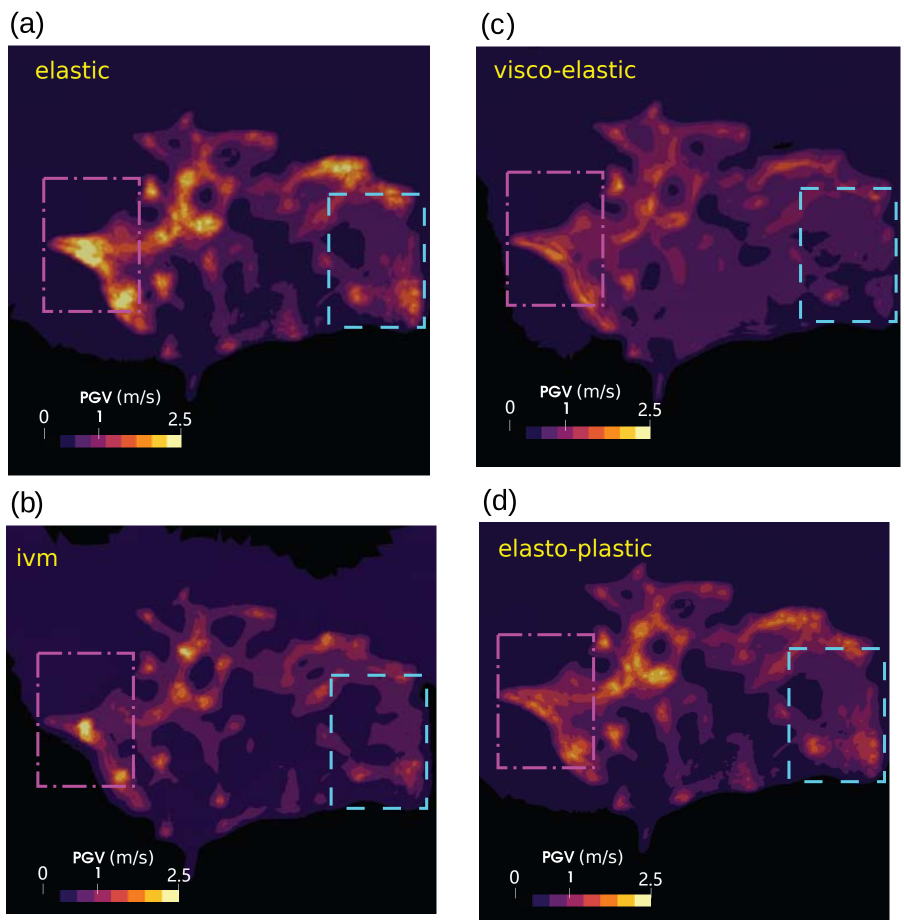

Figure 7. Maps of peak ground velocity (PGV) for different rheologies: (a) elastic, (b) visco-elastic, (c) IVM and (d) elasto-plastic. The dashed blue rectangles highlight the region where the elasto-plastic model exhibits minimal attenuation, while the dash-dotted pink rectangles indicate areas where attenuation is more pronounced.

5 Discussion

5.1 Accuracy and performance of the nonlinear implementation

In Section 4, we applied the proposed algorithm to model regional-scale nonlinear co-seismic wave speed changes in 3D. Nonlinear seismic wave propagation simulations are computationally demanding, necessitating efficient algorithms and optimized implementations for execution on large-scale high-performance computing (HPC) systems (e.g., Reinarz et al., 2020; Roten et al., 2023). To illustrate the efficiency of our nonlinear PDE solver, we analyze its convergence rate with reduced element size h in Section 3.1. We also analyze p convergence in Fig. 1, where the L_2 errors in numerical solutions decrease with element shape functions of higher polynomial degree p.

Fig. 1 shows a first-order convergence rate for simulations using basis functions of polynomial degrees 1 to 5. This low order of convergence results from the linearized Cauchy-Kovalevskaya procedure used in the prediction step, c.f. Eq. (A2). The prediction step approximates the time-dependent coefficients $U_{lp}(t)$ within a single time step using a Taylor series expansion (Toro et al., 2001). In this step, to compute high-order time derivatives, we linearize the nonlinear hyperbolic equations in Eq. (A2) and apply the Cauchy–Kovalevskaya procedure to the linearized system, as detailed in Dumbser and Käser (2006). This linearization ensures algorithmic generality across various nonlinear rock models but limits the accuracy of $U_{lp}(t)$ at higher orders, thus constraining the overall convergence rate.

A low-order convergence rate observed at solution discontinuities, such as shock waves, is consistent with Godunov's theorem (Godunov and Bohachevsky, 1959). This theorem establishes that high-order linear solvers have non-monotonic behavior near steep solution gradients. In addition, spectral convergence properties might be reduced to low-order accuracy due to the manifestation of the well-known Gibbs phenomena in the vicinity of strong discontinuities (e.g., Hesthaven and Warburton, 2007, Chapter 5.6). Local low-order convergence is also evident in SeisSol's dynamic rupture implementation (Sec. 6.3 Wollherr et al., 2018).

A potentially promising extension of our work is the incorporation of a discrete Picard iteration scheme (Lindelöf, 1894; Youssef and El-Arabawy, 2007; Dumbser et al., 2008; Gassner et al., 2011; Reinarz et al., 2020). The Picard iteration can substitute our linearized Cauchy-Kovalevskaya procedure in the prediction step to estimate $\mathcal{D}^i_{lp}$ in Eq. (3). This approach has been shown to help preserve high-order convergence up to 7 in ADER-DG solvers (Dumbser et al., 2008).

We analyze the performance of our SeisSol implementation on the supercomputer Frontera at TACC (Stanzione et al., 2020). Additionally, we suggest potential improvements to enhance the current algorithm, including future large-scale hardware architectures.

We evaluate the scalability and speed-up of the nonlinear SeisSol implementation using the 2015 Kathmandu earthquake model shown in Fig. 4b. We here discretize the simulation domain with three different meshes containing approximately 17, 40, and 100 million elements, respectively. In the discontinuous Galerkin (DG) method, the degrees of freedom (DOFs) are directly proportional to the number of tetrahedral elements. We use a polynomial degree $p = 3$ (Eq. 5) for performance analysis, resulting in 200 DOFs per element.

The scaling tests consist of simulations using all three meshes and various numbers of compute nodes, running for 3 s of physical simulation time with the same time step size. SeisSol employs a hybrid MPI-OpenMP parallelization scheme, utilizing MPI for inter-node communication and OpenMP for multi-threaded parallelization within each node (Uphoff et al., 2017).

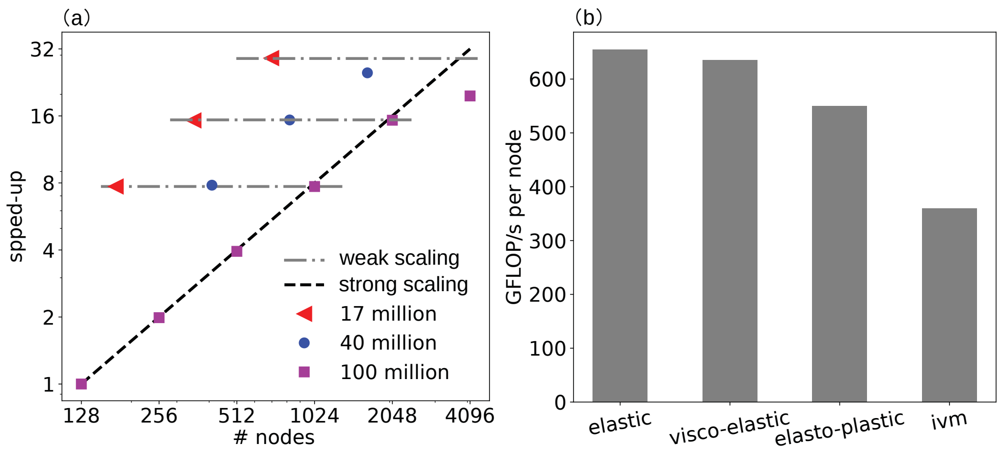

Figure 8. Scalability and performance. (a) Speed-up of simulations as a function of the number of compute nodes, scaling up to 4096 nodes on Frontera (Stanzione et al., 2020). The dashed black curve represents the ideal strong-scaling regime, where doubling the number of nodes halves the time to solution. The dash-dotted gray curves illustrate the ideal weak-scaling regime, where proportionally increasing the number of nodes with the number of mesh elements results in the same speed-up. Different mesh sizes are represented by red triangles (17 million elements), blue circles (40 million elements), and purple rectangles (100 million elements). Both axes use a logarithmic scale. (b) Hardware performance analysis during simulations of the 2015 M_W 7.8 Ghorka earthquake (Section 4) for different rock models, shown as a bar plot. The mesh used here contains ≈2.3 million elements, and the simulation ran on 32 nodes of SuperMUC-NG (Phase 1).

We evaluate the performance in terms of speed-up, which is defined as t_s/t_0 with t_s being the time to solution for a given combination of mesh size and number of compute nodes, t_0 is the time to solution of the baseline simulation which uses a 100-million-element mesh on 128 nodes. Fig. 8 illustrates the scalability on the Frontera supercomputer at TACC (Stanzione et al., 2020). Frontera employs Intel Xeon Platinum 8280 ("Cascade Lake") processors, each offering 56 cores per node and operating at 2.7 GHz. The total number of available compute nodes is 8,368.

We analyze how speed-up depends on mesh sizes and the number of compute nodes in Fig. 8a. To facilitate direct comparison across different mesh sizes for both strong and weak scaling, we normalize the speed-up by nodes per million elements in the following discussions. The results indicate that for fewer than 20 nodes per million elements, strong scaling is nearly linear using the 100 million element mesh, meaning that speed-up increases almost proportionally with node count.

To analyze weak scaling behavior, we compare different mesh sizes using the same number of nodes per million elements. The speed-up across the three different mesh sizes remains nearly identical as long as the number of nodes per million elements remains below 20. However, at 40 nodes per million elements, performance deviates significantly from ideal scaling in both strong and weak scaling tests. Performance degradation becomes more pronounced as the number of elements increases, corresponding to a larger number of compute nodes. One possible explanation is that the communication time between MPI ranks occupies a larger proportion of the overall computation time. Optimizing SeisSol's performance at those higher node counts is beyond the scope of this study and requires further development efforts.

We compare the performance of our implementation using nonlinear space-time interpolation kernels with that of existing SeisSol models. Since our implementation in this work for nonlinear hyperbolic equations only supports a uniform time step size across the entire simulation domain (global time stepping, GTS), we constrain our comparison with the other existing models in SeisSol to the GTS scheme. Uphoff et al. (2017) demonstrate the strong scaling behavior of SeisSol for dynamic rupture earthquake simulations using a linear elastic model. With a mesh containing approximately 51 million elements, the parallel efficiency remained ∼95% on 512 nodes compared to a performance of ∼660 GFLOP/s on 16 nodes. The simulation on 512 nodes corresponds to ∼10 nodes per million elements, which is within the range of our scaling analysis in Fig. 8a.

In terms of strong scaling, our nonlinear implementation reaches a speed-up of ∼15.3 when increasing the number of nodes from 128 to 2048 for a mesh with ∼100 million elements. This result is comparable to the elastic model above, with a parallel efficiency of 95.7% up to ∼20 nodes per million elements. However, when the number of nodes is further increased to 4,096, the parallel efficiency drops to 61.5%, indicating the need for further optimization of our current implementation for handling nonlinear wave propagation at extreme scales. For example, Wolf et al. (2022) recently optimized the implementation of computationally intensive poro-elastic rheologies in SeisSol, achieving performance degradation of less than 10%, even at more than 40 nodes per million elements.

The strong scaling behavior does not fully capture the absolute performance of the code in terms of floating point operations per second (FLOP/s). To provide a more precise assessment, we compare FLOP/s among simulations using the four material models described in Section 4. For a 2.3 million element mesh, performance measurements are taken from results running on 16 nodes of SuperMUC-NG (Phase 1) with shape functions of polynomial degree 3. SuperMUC-NG employs Intel Xeon Platinum 8174 processors, each equipped with 48 cores per node, operating at 2.7 GHz. As shown in Fig. 8b, simulations with elastic, visco-elastic, and elasto-plastic materials achieve a node-average performance of 654 GFLOP/s, 636 GFLOP/s, and 550 GFLOP/s, respectively, using double-precision floating-point arithmetic. In contrast, the nonlinear implementation with IVM achieves 360 GFLOP/s, which represents a 45% reduction in computational performance compared to the elastic model.

The current implementation does not yet support local time stepping (LTS, Breuer et al., 2016; Uphoff, 2020), which is crucial for efficiently handling non-uniform element sizes due to mesh refinement near faults, complex fault geometries, or highly-varying surface topography. Thus, on the same mesh, the time-to-solution for the nonlinear IVM implementation is approximately 5.56 times longer than the linear elastic material in our simulations presented in Section 4. Therefore, future implementation of LTS for nonlinear models is a promising avenue for improving computational efficiency while maintaining accuracy.

5.2 Linking co-seismic wave speed changes of rocks from laboratory measurements to regional scale field observations

In this section, we discuss what the simulations of the 2015 Ghorka earthquake reveal about co-seismic wave speed changes in linking measurements of co-seismic wave speed changes from the laboratory with field-scale observations. Under well-controlled environments and boundary conditions in the laboratory, the dynamic responses of rocks to seismic wave fields can be better constrained. In this work, we employ an experimentally constrained continuum mechanics model, the IVM (Berjamin et al., 2017; Niu et al., 2024). However, the amplitudes of the modeled regional wave speed changes may not be comparable to observations during the 2015 Ghorka earthquake. In the following, we discuss reasons that may contribute to the amplitude difference between the simulated regional co-seismic wave speed changes and those in field observations.

Lu and Ben-Zion (2022) show that the average wave speed changes within a depth range from 0 to ≈3 km can exceed 1% within 90 km from the fault. These changes are two orders of magnitude larger than our simulated wave speed changes at depths of 2 km within 100 km from the fault, which is likely due to large perturbations within soft sediments across the upper few hundred meters below the surface. Such significant perturbations inside the sediments are not reflected in our analysis of a depth slice at 2 km. Fig. 5c shows that wave speed changes within the sedimentary basin reach 88%. Similarly, using seismic observations from the KiK-net network, Bonilla et al. (2019) observe wave speed reductions greater than 60% in shallow soft sediments within 150 s after the occurrence of the 2011 M_W 9.0 Tohoku-oki earthquake in Japan. These results suggest that incorporating the shallowest sedimentary layers may increase the average wave speed changes, potentially enabling a more quantitative comparison between numerical simulations and field observations.

Although this study demonstrates how to adapt laboratory-derived nonlinear models to regional-scale numerical simulations of co-seismic wave speed changes, the nonlinear IVM material properties used in our simulations were not constrained with rock samples from the Kathmandu Valley. However, the spatial variation patterns of co-seismic wave speed changes modeled here may be transferable across similar lithologies. For example, our simulations reveal that the amplitude of co-seismic wave speed changes correlates strongly with fault slip close to the source (Figs. 5a and 4a). At increasing distances from the fault, the dynamic strain amplitude is modulated by the layered Earth model, shown in Fig. 4. With slightly softer rocks (lower c_s in Table 2) at a depth of 2 km, the region where the changes in wave speed are greater than 0.01% is broader than that at a depth of 12 km (Fig. 5a and 5b). This effect is particularly prominent within the sedimentary basin, where low-moduli unconsolidated materials experience greater strain amplification. We find that the basin depth distribution is an additional factor that adds to the spatial variability of changes in nonlinear wave speed. Our results (Fig. 5c) indicate that larger sedimentary basin depths lead to greater co-seismic wave speed reductions. Other factors that might contribute to the variation, for example, the direction of incoming waves (Oral et al., 2022), require further investigation as a next step.

A limitation of our approach is that the nonlinear damage model (IVM) remains isotropic even as damage accumulates. However, material anisotropy may develop under high damage levels (Fig. 3), further influencing directivity effects and path and site effects. Accounting for non-linear anisotropy will introduce additional challenges in accurately implementing free-surface boundary conditions. Although the method outlined in Section A3 is suitable for isotropic models only, it can serve as a first-order approximation for damage- and stress-induced moduli changes at the free-surface boundary by only accounting for the induced changes in the effective Lamé parameters in Eq. (A17).

5.3 Incorporating background stress effects on co-seismic non-linear wave speed changes

In Section 4, we use the IVM with experimentally constrained parameters (Niu et al., 2024) on Westerly granite to quantify the spatial distribution of co-seismic wave speed reductions following the 2015 M_W 7.8 Ghorka earthquake. This model assumes a universal co-seismic wave speed reduction, irrespective of the initial stress state. Similar universal reductions in wave speed under dynamic perturbations have been observed in laboratory rock samples under unconfined stress conditions Remillieux et al. (2017); Feng et al. (2018) and under uniaxial compression of up to 20 MPa (Rivière et al., 2015; Manogharan et al., 2021). However, Manogharan et al. (2022) show that the level of uniaxial compression exerts a second-order influence on the amplitude of co-seismic wave speed reductions, indicating that a more advanced model is needed to incorporate the dependence of wave speed changes on the background stress state.

The CDM (Lyakhovsky et al., 1997a), described in Eq. (3), explicitly accounts for the background stress state. In this model, the amplitude of damage accumulation depends on how close the current stress state is to a critical stress threshold, defined by ξ_0 in Eq. (3). In Section 3.3, we demonstrate that our proposed algorithm can quantify stress- and damage-induced anisotropy in wave propagation using CDM. However, applying CDM to co-seismic wave speed changes requires sufficient knowledge of the pre-existing background stress state.

Properly configuring the background stress state is especially important when modeling layered geological structures, particularly when accounting for spatially varying bathymetry in sedimentary basins (unit 1 in Fig. 4). Using CDM, the background stress state is imposed by specifying the initial strain tensor. To prevent spurious wave generation at the beginning of the simulation, it is necessary to ensure the stress continuity condition at layer boundaries. This is challenging when incorporating geometrically complex basin bathymetry, where the strain tensor must be reoriented according to the basin geometry. A potential solution to this challenge in future work may be first to solve the static strain field resulting from the overburden of rocks and soils. This balanced strain field may then be applied as the initial strain state for wave simulations, ensuring a physically consistent background stress distribution.

6 Conclusions

To develop a seismic wave propagation method capable of modeling observed co-seismic wave speed changes, we propose a generic numerical algorithm based on the discontinuous Galerkin (DG) method that can be applied to a wide range of nonlinear rock models. We verify the numerical solutions obtained using our new approach implemented in the open-source software SeisSol against three sets of analytical solutions and confirm the convergence of the algorithm. Using the Riemann problem setup, we demonstrate that the proposed method accurately resolves discontinuities in nonlinear hyperbolic equations. We find a 1st order convergence rate at solution discontinuities with basis functions of polynomial degrees 1 to 5. On the same mesh, using higher-degree basis functions leads to lower numerical errors. We show that the method can accurately resolve the amplitude of high-frequency harmonics generated by wave propagation in the Murnaghan nonlinear elasticity model. The proposed method can also properly quantify the stress- and damage-induced mechanical anisotropic behaviors of rocks.

We evaluate the parallel performance of our implementation on Frontera and find that both weak and strong scaling remain close to linear up to 20 nodes per million elements, allowing efficient simulations on meshes with up to 100 million elements and scalability up to 2048 nodes. However, despite the good parallel scalability, node-level performance remains non-optimal, indicating the need for further optimizations to improve computational efficiency and reduce runtime for handling future nonlinear wave propagation simulations at extreme scales.

We apply our algorithm to regional-scale earthquake simulations, including nonlinear wave propagation effects from source to site. We use the experimentally constrained nonlinear model IVM to capture co-seismic wave speed changes during the 2015 M_w 7.8 Gorkha earthquake in the Kathmandu Valley, incorporating a free surface with topography, a sedimentary basin with low wave speeds and complex bathymetry, a layered geological structure, and a finite source model that accounts for rupture directivity effects. The simulation results show that co-seismic wave speed reductions depend on the fault slip distribution near the source and are modulated by basin depth tens of kilometers away from the fault. Co-seismic wave speed changes also enhance low-frequency components in soft sedimentary layers, affecting ground motions. This study demonstrates, using a physics-based framework to quantify nonlinear earthquake effects at a regional scale, the importance of damage-induced wave speed variations for seismic hazard assessment, ground motion predictions, and as an observable to better constrain earthquake physics and rock mechanics.

Acknowledgments

The authors thank Dave A. May and Yehuda Ben-Zion for fruitful discussions. We are grateful to Ashim Rijal and Amrit Kaur for their contributions to the Kathmandu model setup. This project has received support from the European Union's Horizon 2020 research and innovation programme under the Marie-Sklodowska-Curie grant agreement No. 955515 – SPIN ITN (www.spin-itn.eu) and the TEAR ERC Starting (grant No. 852992), from Horizon Europe (ChEESE-2P, grant no. 101093038; DT-GEO, grant no. 101058129; and Geo-INQUIRE, grant no. 101058518), the National Science Foundation and TACC's LCCF-CSA (grant numbers OAC-2139536, OAC-2311208, EAR-2225286, EAR-2121568), the National Aeronautics and Space Administration (NASA grant no. 80NSSC20K0495) and the Southern California Earthquake Center (SCEC projects #21112, #22135). The authors acknowledge the Texas Advanced Computing Center (TACC) at The University of Texas at Austin for providing computational resources that have contributed to the research results reported in this paper (http://www.tacc.utexas.edu) and the Gauss Centre for Supercomputing e.V. (www.gauss-centre.eu) for providing computing time on the supercomputer SuperMUC-NG at the Leibniz Supercomputing Centre (www.lrz.de) in project pn49ha. Additional computing resources were provided by the Institute of Geophysics of LMU Munich (Oeser et al., 2006).

Data availability

The source code of SeisSol with nonlinear IVM implementation is available as open-source software under https://github.com/SeisSol/SeisSol/tree/damaged-material-nonlinear-drB. The model setup, simulation outputs, and post-processing scripts to reproduce all figures are available at a Zenodo repository.

Appendix A DG algorithm for nonlinear wave equations

In this section, we provide the details on three components of the DG algorithm proposed in this work: prediction step, correction step, and boundary conditions.

A1 Prediction step: linearization and temporal approximation

In the prediction step, we retain only the conservative term of Eq. (4) assuming weak nonlinearity ($\partial\sigma_{ij}/\partial\varepsilon_{mn}$ and $\partial\sigma_{ij}/\partial\alpha \to$ constant) and employ a linearization procedure. Our main motivation for this linearization in the prediction step is to maintain the HPC-optimized data structure of SeisSol (Uphoff et al., 2024). We will release this restriction in the subsequent correction step described later. This assumption preserves the convergence of the algorithm for nonlinear hyperbolic PDEs but can have an effect on the convergence rate, as we will discuss in Section 3.1.

We write for the linearized prediction step:

$$\begin{aligned}\frac{\partial u_p}{\partial t} &= -\frac{\partial F_p^d}{\partial x_d}\\ &= -\frac{\partial F_p^d}{\partial u_q}\frac{\partial u_q}{\partial x_d},\end{aligned} \tag{A1}$$

where $F_p^d = F_p^d(\underline{u})$ is a nonlinear function of the conservative variables u_p, with $\dfrac{\partial F_p^d}{\partial u_q}$ corresponding to its Jacobian matrix. Taking a time derivative on both sides of Eq. (A1), we approximate the second time derivative of u_p as:

$$\begin{aligned}
\frac{\partial^2 u_p}{\partial t^2} &= -\frac{\partial}{\partial t}\left(\frac{\partial F_p^d}{\partial u_q}\frac{\partial u_q}{\partial x_d}\right) \\
&= -\frac{\partial}{\partial t}\left(\frac{\partial F_p^d}{\partial u_q}\right)\frac{\partial u_q}{\partial x_d} - \frac{\partial F_p^d}{\partial u_q}\frac{\partial}{\partial x_d}\left(\frac{\partial u_q}{\partial t}\right) \\
&\approx -\frac{\partial F_p^d}{\partial u_q}\frac{\partial}{\partial x_d}\left(\frac{\partial u_q}{\partial t}\right).
\end{aligned} \tag{A2}$$

This condition is satisfied if $\frac{\partial}{\partial t}\left(\frac{\partial F_p^d}{\partial u_q}\right)\frac{\partial u_q}{\partial x_d} \ll \frac{\partial F_p^d}{\partial u_q}\frac{\partial}{\partial x_d}\left(\frac{\partial u_q}{\partial t}\right)$, which requires $\frac{\partial F_p^d}{\partial u_q}$ to vary slowly in time compared to the temporal variation of u_q.

From Eqs. (1) and (4), F_p^d incorporates the nonlinear stress-strain relationships. Consequently, $\frac{\partial F_p^d}{\partial u_q}$ changes gradually under weak nonlinearity. The weak nonlinearity makes Eq. (A2) a more accurate approximation for the second-order time derivative of u_p. We reiterate that this assumption only pertains in the prediction step.

Following Uphoff (2020), the arbitrary order (i) derivative of q_p in time ($\mathcal{D}_{lp}^i$) is computed as follows:

$$\mathcal{D}_{lp}^i \int_{\mathcal{T}_m} \phi_k \phi_l \mathrm{d}V = -\int_{\mathcal{T}_m} \phi_k B_{pq}^d(\underline{u}^{t_n}) \mathcal{D}_{lq}^{(i-1)} \frac{\partial \phi_l}{\partial x_d} \mathrm{d}V, \tag{A3}$$

where $\mathcal{D}_{lq}^i \phi_l = \frac{\partial^i u_q}{\partial t^i}$.

For linear wave equations, we derive $B_{pq}^d = \frac{\partial F_p^d}{\partial u_q}$ as a cell-wise constant that keeps its value along the simulation (Uphoff, 2020). In our nonlinear case, we need to re-compute the cell-wise averaged B_{pq}^d from $u_p^{t_n}$ at the beginning of each time step t_n, i.e. $B_{pq}^{d,t_n} = B_{pq}^d(\underline{u}^{t_n}) = \int_{\mathcal{T}_m} B_{pq}^d(\underline{u}^{t_n}) \mathrm{d}V / V_e$ and V_e is the volume of the tetrahedral element.

If we substitute B_{pq}^{d,t_n} in Eq. (A3), the integration in a reference cell $\mathcal{E}_3$, which is defined in a reference Cartesian coordinate system where the position vector of a point is ξ_i, will be

$$\mathcal{D}_{lp}^i |J| \int_{\mathcal{E}_3} \phi_k \phi_l \mathrm{d}V = -|J| \Theta_{ed}^{-1} \mathcal{D}_{lp}^{(i-1)} B_{pq}^{d,t_n} \int_{\mathcal{E}_3} \phi_k \frac{\partial \phi_l}{\partial \xi_e} \mathrm{d}V, \tag{A4}$$

where $\Theta_{ed}^{-1} = \partial \xi_e / \partial x_d$. We refer to Chapter 3.1 of Uphoff (2020) for the detailed definition of the reference Cartesian coordinate system. Defining $M_{kl} = \int_{\mathcal{E}_3} \phi_k \phi_l \mathrm{d}V$ and $K_{lk}^e = \int_{\mathcal{E}_3} \phi_k \frac{\partial \phi_l}{\partial \xi_e} \mathrm{d}V$, we derive

$$\mathcal{D}_{lp}^i |J| M_{kl} = -|J| \Theta_{ed}^{-1} \mathcal{D}_{lq}^{(i-1)} B_{pq}^{d,t_n} K_{lk}^e, \tag{A5}$$

which is directly comparable to Eq.(3.31) in Uphoff (2020).

If the nonlinear source term is considered, we simplify and add the nonlinear source term only when $i = 1$ in Eq. (A5).

$$\mathcal{D}_{lp}^{1}|J|M_{kl} = -|J|\Theta_{ed}^{-1}\mathcal{D}_{lq}^{0}B_{pq}^{d,t_n}K_{lk}^{e} + |J|\int_{\mathcal{E}_3} s_p(\underline{q}^{t_n})\phi_k \mathrm{d}V, \tag{A6}$$

where $u_q^{t_n} = \mathcal{D}_{lq}^{0}\phi_l$, with the same definition of Θ_{ed}^{-1} as Eq. (A4). The nonlinear source function $s_p(\underline{u}^{t_n})$ is evaluated on a nodal basis of $u_q^{t_n}$ projected from the modal basis coefficients $\mathcal{D}_{lq}^{0}$ as presented by Wollherr et al. (2018).

A2 Correction step: time integration and discontinuity handling

The weak form of Eq. (4) with integration by part looks like

$$\frac{\partial}{\partial t}\int_{\mathcal{T}_m}\phi_k U_{lp}(t)\phi_l \mathrm{d}V + \int_{\partial\mathcal{T}_m}\phi_k(F_p^d n_d)^*\mathrm{d}S - \int_{\mathcal{T}_m}\frac{\partial\phi_k}{\partial x_d}F_p^d\mathrm{d}V = \int_{\mathcal{T}_m} s_p(U_{lp}\phi_l)\phi_k\mathrm{d}V, \tag{A7}$$

where $s_p(U_{lp}\phi_l) = (0,0,0,0,0,0,0,0,0,r_\alpha)^T$ as in Eq. (4). n_d is the normal vector of the interface $\partial\mathcal{T}_m$. Integrating both sides of the Eq. (A7) in one time step $[t_n,\, t_{n+1}]$ yields

$$\begin{aligned}\int_{\mathcal{T}_m}\phi_k\phi_l[Q_{lp}^{n+1} - U_{lp}^{n}]\mathrm{d}V + \int_{\partial\mathcal{T}_m}\phi_k\int_{t_n}^{t_{n+1}}(F_p^d n_d)^*\mathrm{d}\tau\mathrm{d}S - \int_{\mathcal{T}_m}\frac{\partial\phi_k}{\partial x_d}\int_{t_n}^{t_{n+1}}F_p^d\mathrm{d}\tau\mathrm{d}V \\ = \int_{\mathcal{T}_m}\phi_k\int_{t_n}^{t_{n+1}}s_p(U_{lp}\phi_l)\mathrm{d}\tau\mathrm{d}V.\end{aligned} \tag{A8}$$

According to Eqs. (5) and (6), we estimate the space-time integration in each term of Eq. (A8) with $\mathcal{D}_{lp}^{i}$ derived from the prediction step.

We expand on the space-time integration term by term in the following. We start from the second term on the left-hand-side of Eq. (A8) when $\partial\mathcal{T}_m$ is on the element surfaces that are not on the boundaries of the computation domain. The latter case will be addressed in Section A3. The interface flux within the computational domain $(F_p^d n_d)^*$ must account for the solution discontinuities on each side of the interface. Strictly speaking, this requires solving the Riemann problem for a nonlinear hyperbolic system (LeVeque, 2002). Here we use the local Lax-Friedrich flux F_p^{LF} which has a simple form while preserving numerical stability. Its expression is

$$\begin{aligned}F_p^{LF} &= (F_p^d n_d)_p^* \\ &= \frac{1}{2}(F_p^d(u_p^+) + F_p^d(u_p^-))n_d + \frac{1}{2}C(u_p^- - u_p^+),\end{aligned} \tag{A9}$$

where C is the largest eigenvalues of the matrix $B_{pq}^d((\underline{u}^+ + \underline{u}^-)/2)$ in Eq. (A3). As defined in Eq. (A9), F_p^{LF} is a nonlinear function of u_p on both sides of u_p^+ and u_p^-. For the numerical integration, we evaluate F_p^{LF} at the quadrature points in space and time following Uphoff (2020) and expand the second term on the left-hand-side of Eq. (A8) as

$$\begin{aligned}&\int_{\partial\mathcal{T}_m}\phi_k\int_{t_n}^{t_{n+1}}(F_p^d n_d)^*\mathrm{d}\tau\mathrm{d}S \\ &= \sum_{i=1}^{N^s}\beta_i\phi_{k,i}\sum_{z=1}^{N^t}\gamma_z F_{lp,z,s}^{LF}|S_f|\Delta t,\end{aligned} \tag{A10}$$

where β_i and γ_z are weights, respectively, for surface and time integration.

For the third term on the left-hand-side of Eq. (A8), we also discretize $F_p^d = \mathcal{F}_{lp}^d(t)\phi_l(\boldsymbol{x})$ with the same modal basis functions as u_p. We briefly summarize the procedures here and refer to Wollherr et al. (2018) for the detailed formulae. The evaluation of $\mathcal{F}_{lp}^d(t)$ follows 3 steps: (1) Project $U_{lp}(t)$ into a nodal basis and obtain the $U_{lp}^{Node}(t)$ coefficients in the nodal basis; (2) Evaluate the coefficients $\mathcal{F}_{lp}^{d,Node}$ in nodal space by substituting $U_{lp}^{Node}(t)$ into the nonlinear function $\mathcal{F}_p^d(U_{lp}^{Node})$ based on Eq. (1) to Eq. (3); (3) Obtain the coefficients $\mathcal{F}_{lp}^d(t)$ in modal space by projecting back from the nodal space coefficients $\mathcal{F}_p^d(U_{lp}^{Node})$. The third term on the left-hand-side of Eq. (A8) then becomes

$$
\begin{aligned}
&\int_{\mathcal{T}_m} \frac{\partial \phi_k}{\partial x_d} \int_{t_n}^{t_{n+1}} F_p^d \mathrm{d}\tau \mathrm{d}V \\
=& \int_{t_n}^{t_{n+1}} \mathcal{F}_{lp}^d(\tau)\mathrm{d}\tau \int_{\mathcal{T}_m} \frac{\partial \phi_k}{\partial x_d} \phi_l \mathrm{d}V.
\end{aligned}
\tag{A11}
$$

We employ a similar procedure for the right-hand-side of Eq. (A8). We discretize $s_p(t) = S_{lp}(t)\phi_l$ and yield

$$
\begin{aligned}
&\int_{\mathcal{T}_m} \phi_k \int_{t_n}^{t_{n+1}} s_p(U_{lp}\phi_l)\mathrm{d}\tau \mathrm{d}V \\
=& \int_{t_n}^{t_{n+1}} S_{lp}(\tau)\mathrm{d}\tau \int_{\mathcal{T}_m} \phi_k \phi_l \mathrm{d}V.
\end{aligned}
\tag{A12}
$$

A3 Free surface and absorbing boundary conditions

We need to take care of the numerical flux $(F_p^d n_d)^*$ in the second term of Eq. (A8) when $\partial\mathcal{T}_m$ is defined on two types of boundaries that are important for earthquake simulations: the absorbing boundary and the free-surface boundary. While IVM in Eq. (2) remains isotropic with damage accumulation, CDM in Eq. (3) can introduce stress-induced anisotropic mechanical responses in rocks (Hamiel et al., 2009). Such anisotropy inside the bulk materials can be resolved using the local Lax-Friedrich flux in Eq. (A9) (de la Puente et al., 2007). In defining the boundary conditions of the simulation domain, we simplify by only considering the nonlinear effects on the isotropic moduli, i.e., the two Lamé parameters. To achieve this, we retain only the components of $\underline{\underline{B}}^d = B_{pq}^d$ that correspond to the isotropic effective Lamé parameters, denoting an approximated matrix as $\underline{\underline{B}}^{d,eff}$. The expressions for $\underline{\underline{B}}^{d,eff}$ are (Wilcox et al., 2010):

$$
\underline{\underline{B}}^{1,eff} =
\begin{bmatrix}
0 & 0 & 0 & 0 & 0 & 0 & -1 & 0 & 0 & 0 \\
0 & 0 & 0 & 0 & 0 & 0 & 0 & 0 & 0 & 0 \\
0 & 0 & 0 & 0 & 0 & 0 & 0 & 0 & 0 & 0 \\
0 & 0 & 0 & 0 & 0 & 0 & 0 & -\frac{1}{2} & 0 & 0 \\
0 & 0 & 0 & 0 & 0 & 0 & 0 & 0 & 0 & 0 \\
0 & 0 & 0 & 0 & 0 & 0 & 0 & 0 & -\frac{1}{2} & 0 \\
-\frac{\lambda^{eff} + 2\mu^{eff}}{\rho} & -\frac{\lambda^{eff}}{\rho} & -\frac{\lambda^{eff}}{\rho} & 0 & 0 & 0 & 0 & 0 & 0 & 0 \\
0 & 0 & 0 & -\frac{2\mu^{eff}}{\rho} & 0 & 0 & 0 & 0 & 0 & 0 \\
0 & 0 & 0 & 0 & 0 & -\frac{2\mu^{eff}}{\rho} & 0 & 0 & 0 & 0 \\
0 & 0 & 0 & 0 & 0 & 0 & 0 & 0 & 0 & 1
\end{bmatrix},
\tag{A13}
$$

$$
\underset{=}{B}^{2,eff} = \begin{bmatrix}
0 & 0 & 0 & 0 & 0 & 0 & 0 & 0 & 0 & 0 \\
0 & 0 & 0 & 0 & 0 & 0 & 0 & -1 & 0 & 0 \\
0 & 0 & 0 & 0 & 0 & 0 & 0 & 0 & 0 & 0 \\
0 & 0 & 0 & 0 & 0 & 0 & -\frac{1}{2} & 0 & 0 & 0 \\
0 & 0 & 0 & 0 & 0 & 0 & 0 & 0 & -\frac{1}{2} & 0 \\
0 & 0 & 0 & 0 & 0 & 0 & 0 & 0 & 0 & 0 \\
0 & 0 & 0 & -\frac{2\mu^{eff}}{\rho} & 0 & 0 & 0 & 0 & 0 & 0 \\
-\frac{\lambda^{eff}+2\mu^{eff}}{\rho} & -\frac{\lambda^{eff}}{\rho} & -\frac{\lambda^{eff}}{\rho} & 0 & 0 & 0 & 0 & 0 & 0 & 0 \\
0 & 0 & 0 & 0 & -\frac{2\mu^{eff}}{\rho} & 0 & 0 & 0 & 0 & 0 \\
0 & 0 & 0 & 0 & 0 & 0 & 0 & 0 & 0 & 1
\end{bmatrix}, \tag{A14}
$$

$$
\underset{=}{B}^{3,eff} = \begin{bmatrix}
0 & 0 & 0 & 0 & 0 & 0 & 0 & 0 & 0 & 0 \\
0 & 0 & 0 & 0 & 0 & 0 & 0 & 0 & 0 & 0 \\
0 & 0 & 0 & 0 & 0 & 0 & 0 & 0 & -1 & \\
0 & 0 & 0 & 0 & 0 & 0 & 0 & 0 & 0 & 0 \\
0 & 0 & 0 & 0 & 0 & 0 & 0 & -\frac{1}{2} & 0 & 0 \\
0 & 0 & 0 & 0 & 0 & 0 & -\frac{1}{2} & 0 & 0 & 0 \\
0 & 0 & 0 & 0 & 0 & -\frac{2\mu^{eff}}{\rho} & 0 & 0 & 0 & 0 \\
0 & 0 & 0 & 0 & -\frac{2\mu^{eff}}{\rho} & 0 & 0 & 0 & 0 & 0 \\
-\frac{\lambda^{eff}}{\rho} & -\frac{\lambda^{eff}+2\mu^{eff}}{\rho} & -\frac{\lambda^{eff}}{\rho} & 0 & 0 & 0 & 0 & 0 & 0 & 0 \\
0 & 0 & 0 & 0 & 0 & 0 & 0 & 0 & 0 & 1
\end{bmatrix}. \tag{A15}
$$

The effective Lamé parameters for IVM are

$$
\begin{cases} \lambda^{eff} = (1-\alpha)\lambda_0 \\ \mu^{eff} = (1-\alpha)\mu_0 \end{cases} . \tag{A16}
$$

The effective Lamé parameters for CDM are

$$
\begin{cases} \lambda^{eff} = \lambda_0 - \alpha\gamma_r\epsilon/\sqrt{I_2} \\ \mu^{eff} = \mu_0 - \alpha\xi_0\gamma_r - 0.5\alpha\gamma_r\xi \end{cases} , \tag{A17}
$$

where $\epsilon = (\varepsilon_{xx} + \varepsilon_{yy} + \varepsilon_{zz})/3$.

We compute the numerical fluxes $(F_p^d n_d)^*$ on both the absorbing boundary and the free-surface boundary based on the solutions of the Riemann problem with an upwind method using the approximate effective matrix $\underset{=}{B}^{d,eff}$ defined in Eq. (A13) to (A15). We assume that the outgoing waves at the element interface are only influenced by the state in the element that the interface belongs to; the incoming waves at the element interface are only influenced by the state in the neighboring element.

To compute the upwind flux, we diagonalize matrix $\underline{\underline{B}}^{1,eff} = \underline{\underline{R}}\,\underline{\underline{\Lambda}}\,\underline{\underline{R}}^{-1}$, where $\underline{\underline{\Lambda}} = \mathrm{diag}(-c_p^{eff}, -c_s^{eff}, -c_s^{eff}, 0, 0, 0, c_s^{eff}, c_s^{eff}, c_p^{eff}, 0)$, $c_p^{eff} = \sqrt{(\lambda_{eff} + 2\mu_{eff})/\rho}$, $c_p^{eff} = \sqrt{\mu_{eff}/\rho}$, and

$$\underline{\underline{R}} = \begin{bmatrix} 1 & 0 & 0 & -\dfrac{\lambda^{eff}}{\lambda^{eff}+2\mu^{eff}} & 0 & -\dfrac{\lambda^{eff}}{\lambda^{eff}+2\mu^{eff}} & 0 & 0 & -1 & 0 \\ 0 & 0 & 0 & 0 & 0 & 1 & 0 & 0 & 0 & 0 \\ 0 & 0 & 0 & 1 & 0 & 0 & 0 & 0 & 0 & 0 \\ 0 & \dfrac{1}{2} & 0 & 0 & 0 & 0 & 0 & -\dfrac{1}{2} & 0 & 0 \\ 0 & 0 & 0 & 0 & 1 & 0 & 0 & 0 & 0 & 0 \\ 0 & 0 & \dfrac{1}{2} & 0 & 0 & 0 & -\dfrac{1}{2} & 0 & 0 & 0 \\ c_p^{eff} & 0 & 0 & 0 & 0 & 0 & 0 & 0 & c_p^{eff} & 0 \\ 0 & c_s^{eff} & 0 & 0 & 0 & 0 & 0 & c_s^{eff} & 0 & 0 \\ 0 & 0 & c_s^{eff} & 0 & 0 & 0 & c_s^{eff} & 0 & 0 & 0 \\ 0 & 0 & 0 & 0 & 0 & 0 & 0 & 0 & 0 & 1 \end{bmatrix}, \tag{A18}$$

where the last column results from the extra zero eigenvalues due to the introduction of the damage variable.

For the absorbing boundaries, we use the same method as Dumbser and Käser (2006).

$$\begin{aligned} F_p^{abs} &= (F_p^d n_d)_p^* \\ &= T_{pq} B_{qr}^{1,eff,+} T_{rs}^{-1} q_s, \end{aligned} \tag{A19}$$

where $\underline{\underline{B}}^{1,eff,+} = \underline{\underline{R}}\,\underline{\underline{\Lambda}}^{+}\underline{\underline{R}}^{-1}$. $\underline{\underline{\Lambda}}^{+} = \mathrm{diag}(0, 0, 0, 0, 0, 0, c_s^{eff}, c_s^{eff}, c_p^{eff}, 0)$ only keeps the positive terms in $\underline{\underline{\Lambda}}$. T_{pq}^{-1} is the rotation matrix that operates on the vector of the conservative variables u_s, rotating the quantities to the face-aligned coordinate system.

$$\underline{\underline{T}} = \begin{bmatrix} n_x^2 & s_x^2 & t_x^2 & 2n_x s_x & 2s_x t_x & 2t_x n_x & 0 & 0 & 0 & 0 \\ n_y^2 & s_y^2 & t_y^2 & 2n_y s_y & 2s_y t_y & 2t_y n_y & 0 & 0 & 0 & 0 \\ n_z^2 & s_z^2 & t_z^2 & 2n_z s_z & 2s_z t_z & 2t_z n_z & 0 & 0 & 0 & 0 \\ n_x n_y & s_x s_y & t_x t_y & n_x s_y + n_y s_x & t_x s_y + t_y s_x & n_x t_y + n_y t_x & 0 & 0 & 0 & 0 \\ n_z n_y & s_z s_y & t_z t_y & n_z s_y + n_y s_z & t_z s_y + t_y s_z & n_z t_y + n_y t_z & 0 & 0 & 0 & 0 \\ n_x n_z & s_x s_z & t_x t_z & n_x s_z + n_z s_x & t_x s_z + t_z s_x & n_x t_z + n_z t_x & 0 & 0 & 0 & 0 \\ 0 & 0 & 0 & 0 & 0 & 0 & n_x & s_x & t_x & 0 \\ 0 & 0 & 0 & 0 & 0 & 0 & n_y & s_y & t_y & 0 \\ 0 & 0 & 0 & 0 & 0 & 0 & n_z & s_z & t_z & 0 \\ 0 & 0 & 0 & 0 & 0 & 0 & 0 & 0 & 0 & 1 \end{bmatrix}. \tag{A20}$$

For the free-surface boundaries, we first rotate u_q to the face-aligned coordinate system as $u_p^n = T_{rs}^{-1} u_s$. We then derive the constraints to the conservative variables u_q^b on the boundary face from an upwind flux below in a similar way as Uphoff (2020).

$$
\begin{aligned}
\underline{u}^b &= \underline{u}^- + \omega_1 \underline{r}^1 + \omega_2 \underline{r}^2 + \omega_3 \underline{r}^3 \\
&= \underline{u}^- + \omega_1 \begin{pmatrix} 1 \\ 0 \\ 0 \\ 0 \\ 0 \\ 0 \\ c_p^{eff} \\ 0 \\ 0 \\ 0 \end{pmatrix} + \omega_2 \begin{pmatrix} 0 \\ 0 \\ 0 \\ 1/2 \\ 0 \\ 0 \\ 0 \\ c_s^{eff} \\ 0 \\ 0 \end{pmatrix} + \omega_3 \begin{pmatrix} 0 \\ 0 \\ 0 \\ 0 \\ 0 \\ 1/2 \\ 0 \\ 0 \\ c_s^{eff} \\ 0 \end{pmatrix},
\end{aligned}
\tag{A21}
$$

where $\underline{u}^-$ is the projection of solutions in the local element on the free surface; $\underline{r}^1$ is the column in $\underline{\underline{R}}$ that corresponds to -c_p^{eff} in $\underline{\underline{\Lambda}}$; $\underline{r}^2$ and $\underline{r}^3$ are the two columns in $\underline{\underline{R}}$ that correspond to -c_s^{eff} in $\underline{\underline{\Lambda}}$. ω_1, ω_2 and ω_3 are unknowns to be constrained from the free-surface boundary conditions, which we will further define below.

We derive from u_p^b the face-aligned boundary stress $u_p^{\sigma,b} = (\sigma_{xx}, \sigma_{yy}, \sigma_{zz}, \sigma_{xy}, \sigma_{yz}, \sigma_{zx}, v_x, v_y, v_z, \alpha)^T$, where

$$
\begin{aligned}
u_p^{\sigma,b} &= C_{pq} u_q^b \\
&= \begin{bmatrix}
\lambda^{eff} + 2\mu^{eff} & \lambda^{eff} & \lambda^{eff} & & 0 & 0 & \\
\lambda^{eff} & \lambda^{eff} + 2\mu^{eff} & \lambda^{eff} & 0 & 0 & 1 & \\
\lambda^{eff} & \lambda^{eff} & \lambda^{eff} + 2\mu^{eff} & 0 & 0 & 0 & \underline{\underline{0}} \\
0 & 0 & 0 & 2\mu^{eff} & 0 & 0 & \\
0 & 0 & 0 & 0 & 2\mu^{eff} & 0 & \\
0 & 0 & 0 & 0 & 0 & 2\mu^{eff} & \\
 & & \underline{0} & & & & \underline{\underline{I}}
\end{bmatrix} \underline{u}^b,
\end{aligned}
\tag{A22}
$$

where $\underline{\underline{I}}$ is a 4 by 4 identity matrix, while $\underline{\underline{0}}$ and $\underline{0}$ are, respectively, the zero matrix and zero vector that complete the matrix C_{pq}.

On the free surface, σ_{xx}, σ_{xy} and σ_{zx} in $u_p^{\sigma,b}$ should be zero. With these three more constraints, we solve the unknowns ω_1, ω_2 and ω_3 in Eq. (A21). We can substitute these unknowns back in Eq. (A21) to obtain u_q^b in the face-aligned coordinate system. We finally compute the boundary flux with u_q^b as below.

$$
\begin{aligned}
F_p^{free} &= (F_p^d n_d)_p^* \\
&= T_{pq} B_{qr}^{1,eff} u_r^b.
\end{aligned}
\tag{A23}
$$

Appendix B Frequency components of the ground motion recorded at different stations inside the Kathmandu Valley

This section provides supporting information for reproducing the low-frequency enhancement observed in ground motions from our simulations using the nonlinear damage model, IVM. We present comparisons between the frequency components of the velocity time series predicted by the elastic model and the IVM at four additional strong motion stations within the Kathmandu Valley, as shown in Fig. B1. Among the four listed stations, we find a prominent low-frequency enhancement in the simulations with IVM between 0.2 Hz and 0.35 Hz at station TVU and between 0.3 Hz and 0.45 Hz at station

KATNP. In contrast, the frequency spectra at stations THM and PTN show negligible differences between simulations using the linear elastic model and those with IVM. peak ground velocity (PGV) is strongly correlated with the prominence of the low-frequency enhancement. Specifically, the PGV at station TVU and KATNP is approximately twice and four times higher, respectively, than at station THM. The PGV at the station PTN is approximately 60% larger than that at station THM. With such an intermediate PGV value, only a minor low-frequency enhancement between 0.25 Hz and 0.4 Hz is observed at station PTN. The more prominent low-frequency enhancement associated with larger PGV is attributed to the stronger reduction in co-seismic moduli in regions with high PGV values.

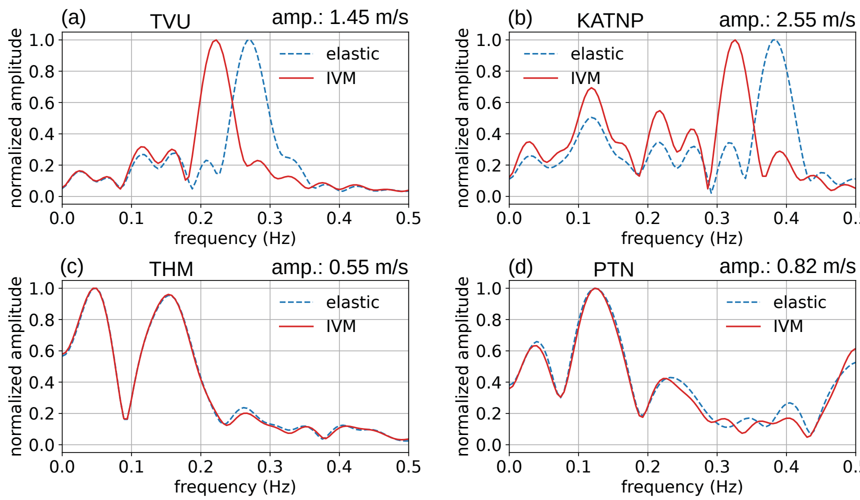

Figure B1. Normalized frequency spectra of the upward-downward velocity time series recorded between 20 s and 50 s for simulations employing elastic model (the dashed blue curve) and IVM (the solid red curve) at 4 stations: (a) TVU, (b) KATNP, (c) THM, and (d) PTN. We provide peak magnitudes of the velocity vector at the four stations on the top right of each sub-figure.

References

Ben-Zion, Y., Beroza, G.C., Bohnhoff, M., Gabriel, A.A., Mai, P.M., 2022. A grand challenge international infrastructure for earthquake science.

Berjamin, H., Favrie, N., Lombard, B., Chiavassa, G., 2017. Nonlinear waves in solids with slow dynamics: an internal-variable model. Proceedings of the Royal Society A: Mathematical, Physical and Engineering Sciences 473, 20170024.

Berjamin, H., Lombard, B., Chiavassa, G., Favrie, N., 2019. Plane-strain waves in nonlinear elastic solids with softening. Wave Motion 89, 65–78.

Boatwright, J., Boore, D.M., 1982. Analysis of the ground accelerations radiated by the 1980 Livermore Valley earthquakes for directivity and dynamic source characteristics. Bulletin of the Seismological Society of America 72, 1843–1865.

Bohara, P., Ghimire, S., 2015. Analysis of shallow seismic waves to determine geotechnical characterization of major earthquake affected sites of Kathmandu valley, in: Proceedings of IOE Graduate Conference, pp. 63–68.

Bokelmann, G.H., Harjes, H.P., 2000. Evidence for temporal variation of seismic velocity within the upper continental crust. Journal of Geophysical Research: Solid Earth 105, 23879–23894.

Bonilla, L.F., Ben-Zion, Y., 2021. Detailed space–time variations of the seismic response of the shallow crust to small earthquakes from analysis of dense array data. Geophysical Journal International 225, 298–310.

Bonilla, L.F., Guéguen, P., Ben-Zion, Y., 2019. Monitoring coseismic temporal changes of shallow material during strong ground motion with interferometry and autocorrelation. Bulletin of the Seismological Society of America 109, 187–198.

Bonilla, L.F., Tsuda, K., Pulido, N., Régnier, J., Laurendeau, A., 2011. Nonlinear site response evidence of K-NET and KiK-net records from the 2011 off the Pacific coast of Tohoku Earthquake. Earth, planets and space 63, 785–789.

Bouchon, M., 1997. The state of stress on some faults of the san andreas system as inferred from near-field strong motion data. Journal of Geophysical Research: Solid Earth 102, 11731–11744.

Brenguier, F., Campillo, M., Takeda, T., Aoki, Y., Shapiro, N., Briand, X., Emoto, K., Miyake, H., 2014. Mapping pressurized volcanic fluids from induced crustal seismic velocity drops. Science 345, 80–82.

Brenguier, F., Shapiro, N.M., Campillo, M., Ferrazzini, V., Duputel, Z., Coutant, O., Nercessian, A., 2008. Towards forecasting volcanic eruptions using seismic noise. Nature Geoscience 1, 126–130.

Breuer, A., Heinecke, A., Bader, M., 2016. Petascale local time stepping for the ader-dg finite element method, in: 2016 IEEE international parallel and distributed processing symposium (IPDPS), IEEE. pp. 854–863.

Browning, J., Meredith, P.G., Stuart, C., Healy, D., Harland, S., Mitchell, T.M., 2017. Acoustic characterization of crack damage evolution in sandstone deformed under conventional and true triaxial loading. Journal of Geophysical Research: Solid Earth 122, 4395–4412.

Butcher, J., 2007. Runge-Kutta methods. Scholarpedia 2, 3147.

Carcione, J.M., Kosloff, D., Kosloff, R., 1988. Wave propagation simulation in a linear viscoelastic medium. Geophysical Journal International 95, 597–611.

Carrington, L., Komatitsch, D., Laurenzano, M., Tikir, M.M., Michéa, D., Le Goff, N., Snavely, A., Tromp, J., 2008. High-frequency simulations of global seismic wave propagation using SPECFEM3D_GLOBE on 62k processors, in: SC'08: Proceedings of the 2008 ACM/IEEE Conference on Supercomputing, IEEE. pp. 1–11.

Castellaro, S., Musinu, G., 2023. Resonance versus shape of sedimentary basins. Bulletin of the Seismological Society of America 113, 745–761.

Castro-Cruz, D., Regnier, J., Bertrand, E., Courboulex, F., 2020. A new parameter to empirically describe and predict the non-linear seismic response of sites derived from the analysis of Kik-Net database. Soil Dynamics and Earthquake Engineering 128, 105833.

Causse, M., Dalguer, L., Mai, P.M., 2014. Variability of dynamic source parameters inferred from kinematic models of past earthquakes. Geophysical Journal International 196, 1754–1769.

Cockburn, B., Karniadakis, G.E., Shu, C.W., 2012. Discontinuous Galerkin methods: theory, computation and applications. volume 11. Springer Science & Business Media.

Cockburn, B., Shu, C.W., 1989. TVB Runge-Kutta local projection discontinuous Galerkin finite element method for conservation laws. ii. general framework. Mathematics of computation 52, 411–435.

Cui, Y., Olsen, K.B., Jordan, T.H., Lee, K., Zhou, J., Small, P., Roten, D., Ely, G., Panda, D.K., Chourasia, A., et al., 2010. Scalable earthquake simulation on petascale supercomputers, in: SC'10: Proceedings of the 2010 ACM/IEEE International Conference for High Performance Computing, Networking, Storage and Analysis, IEEE. pp. 1–20.

Delsanto, P.P., Scalerandi, M., 2003. Modeling nonclassical nonlinearity, conditioning, and slow dynamics effects in mesoscopic elastic materials. Physical Review B 68, 064107.

Desmorat, R., 2016. Anisotropic damage modeling of concrete materials. International Journal of Damage Mechanics 25, 818–852.

Dumbser, M., Balsara, D.S., Toro, E.F., Munz, C.D., 2008. A unified framework for the construction of one-step finite volume and discontinuous Galerkin schemes on unstructured meshes. Journal of Computational Physics 227, 8209–8253.

Dumbser, M., Käser, M., 2006. An arbitrary high-order discontinuous Galerkin method for elastic waves on unstructured meshes–II. the three-dimensional isotropic case. Geophysical Journal International 167, 319–336.

Esmaeilzadeh, A., Motazedian, D., Hunter, J., 2019. 3d nonlinear ground-motion simulation using a physics-based method for the kinburn basin. Bulletin of the Seismological Society of America 109, 1282–1311.

Fan, W., Shearer, P.M., 2015. Detailed rupture imaging of the 25 April 2015 Nepal earthquake using teleseismic P waves. Geophysical Research Letters 42, 5744–5752.

Feng, X., Fehler, M., Brown, S., Szabo, T.L., Burns, D., 2018. Short-period nonlinear viscoelastic memory of rocks revealed by copropagating longitudinal acoustic waves. Journal of Geophysical Research: Solid Earth 123, 3993–4006.

Gabriel, A.A., Li, D., Chiocchetti, S., Tavelli, M., Peshkov, I., Romenski, E., Dumbser, M., 2021. A unified first-order hyperbolic model for nonlinear dynamic rupture processes in diffuse fracture zones. Philosophical Transactions of the Royal Society A 379, 20200130.

Gassenmeier, M., Sens-Schönfelder, C., Eulenfeld, T., Bartsch, M., Victor, P., Tilmann, F., Korn, M., 2016. Field observations of seismic velocity changes caused by shaking-induced damage and healing due to mesoscopic nonlinearity. Geophysical Journal International 204, 1490–1502.

Gassner, G., Dumbser, M., Hindenlang, F., Munz, C.D., 2011. Explicit one-step time discretizations for discontinuous galerkin and finite volume schemes based on local predictors. Journal of Computational Physics 230, 4232–4247.

van Ginkel, J., Ruigrok, E., Wentinck, R., Herber, R., 2022. Amplification behaviour of compressional waves in unconsolidated sediments. Frontiers in Earth Science 10, 812658.

Godunov, S.K., Bohachevsky, I., 1959. Finite difference method for numerical computation of discontinuous solutions of the equations of fluid dynamics. Matematičeskij sbornik 47, 271–306.

Hamiel, Y., Lyakhovsky, V., Stanchits, S., Dresen, G., Ben-Zion, Y., 2009. Brittle deformation and damage-induced seismic wave anisotropy in rocks. Geophysical Journal International 178, 901–909.

Harris, R.A., Barall, M., Archuleta, R., Dunham, E., Aagaard, B., Ampuero, J.P., Bhat, H., Cruz-Atienza, V., Dalguer, L., Dawson, P., et al., 2009. The scec/usgs dynamic earthquake rupture code verification exercise. Seismological Research Letters 80, 119–126.

Hartzell, S., Meremonte, M., Ramírez-Guzmán, L., McNamara, D., 2014. Ground motion in the presence of complex topography: Earthquake and ambient noise sources. Bulletin of the Seismological Society of America 104, 451–466.

Heinecke, A., Breuer, A., Rettenberger, S., Bader, M., Gabriel, A., Pelties, C., Bode, A., Barth, W., Liao, X., Vaidyanathan, K., Smelyanskiy, M., Dubey, P., 2014a. Petascale High Order Dynamic Rupture Earthquake Simulations on Heterogeneous Supercomputers, in: SC14: Proceedings of the International Conference for High Performance Computing, Networking, Storage and Analysis, pp. 3–14. doi:10.1109/SC.2014.6.

Heinecke, A., Breuer, A., Rettenberger, S., Bader, M., Gabriel, A.A., Pelties, C., Bode, A., Barth, W., Liao, X.K., Vaidyanathan, K., et al., 2014b. Petascale high order dynamic rupture earthquake simulations on heterogeneous supercomputers, in: SC'14: Proceedings of the International Conference for High Performance Computing, Networking, Storage and Analysis, IEEE. pp. 3–14.

Hesthaven, J.S., Warburton, T., 2007. Nodal discontinuous Galerkin methods: algorithms, analysis, and applications. Springer Science & Business Media.

Ilsche, T., Schöne, R., Schuchart, J., Hackenberg, D., Simon, M., Georgiou, Y., Nagel, W.E., 2019. Power measurement techniques for energy-efficient computing: reconciling scalability, resolution, and accuracy. SICS Software-Intensive Cyber-Physical Systems 34, 45–52.

Iwan, W.D., 1967. On a class of models for the yielding behavior of continuous and composite systems. Journal of Applied Mechanics 34, 612–617.

Jiao, J., Li, Z., Li, L., Li, G., Lu, X., 2025. Nondestructive evaluation of adhesive joints using nonlinear non-collinear wave mixing technique. Journal of Nondestructive Evaluation 44, 1–15.

Johnson, P., Sutin, A., 2005. Slow dynamics and anomalous nonlinear fast dynamics in diverse solids. The Journal of the Acoustical Society of America 117, 124–130.

Johnson, P.A., Rasolofosaon, P.N., 1993. Nonlinear elasticity and stress-induced anisotropy in rocks: reflections on experimental results, in: SEG Technical Program Expanded Abstracts 1993. Society of Exploration Geophysicists, pp. 792–795.

Kachanov, L., 1986. Introduction to continuum damage mechanics. volume 10. Springer Science & Business Media.

Käser, M., Dumbser, M., De La Puente, J., Igel, H., 2007. An arbitrary high-order discontinuous galerkin method for elastic waves on unstructured meshes—iii. viscoelastic attenuation. Geophysical Journal International 168, 224–242.

Kojima, K., Takewaki, I., 2016. Closed-form critical earthquake response of elastic–plastic structures on compliant ground under near-fault ground motions. Frontiers in Built Environment 2, 1.

Kovalevskaja, S.V., 1874. Zur Theorie der partiellen Differentialgleichungen.

Kramer, S.L., Stewart, J.P., 2024. Geotechnical earthquake engineering. CRC Press.

Krenz, L., Uphoff, C., Ulrich, T., Gabriel, A.A., Abrahams, L.S., Dunham, E.M., Bader, M., 2021. 3d acoustic-elastic coupling with gravity: the dynamics of the 2018 palu, sulawesi earthquake and tsunami, in: Proceedings of the International Conference for High Performance Computing, Networking, Storage and Analysis, pp. 1–14.

Landau, L.D., Lifšic, E.M., Lifshitz, E.M., Kosevich, A.M., Pitaevskii, L.P., 1986. Theory of elasticity: volume 7. volume 7. Elsevier.

Lax, P.D., 2005. Weak solutions of nonlinear hyperbolic equations and their numerical computation, in: Selected Papers Volume I. Springer, pp. 198–232.

Lebedev, A., Ostrovsky, L., 2014. A unified model of hysteresis and long-time relaxation in heterogeneous materials. Acoustical Physics 60, 555–561.

Lee, S.J., Komatitsch, D., Huang, B.S., Tromp, J., 2009. Effects of topography on seismic-wave propagation: An example from northern Taiwan. Bulletin of the Seismological Society of America 99, 314–325.

LeVeque, R.J., 2002. Finite volume methods for hyperbolic problems. volume 31. Cambridge university press.

Li, G., Ben-Zion, Y., 2023. Daily and seasonal variations of shallow seismic velocities in southern California from joint analysis of H/V ratios and autocorrelations of seismic waveforms. Journal of Geophysical Research: Solid Earth 128, e2022JB025682.

Lindelöf, E., 1894. Sur l'application de la méthode des approximations successives aux équations différentielles ordinaires du premier ordre. Comptes rendus hebdo-

madaires des séances de l'Académie des sciences 116, 454–457.
Lu, Y., Ben-Zion, Y., 2022. Regional seismic velocity changes following the 2019 M_W 7.1 Ridgecrest, California earthquake from autocorrelations and P/S converted waves. Geophysical Journal International 228, 620–630.
Lyakhovsky, V., Ben-Zion, Y., Agnon, A., 1997a. Distributed damage, faulting, and friction. Journal of Geophysical Research: Solid Earth 102, 27635–27649.
Lyakhovsky, V., Ben-Zion, Y., Ilchev, A., Mendecki, A., 2016. Dynamic rupture in a damage-breakage rheology model. Geophysical Journal International 206, 1126–1143.
Lyakhovsky, V., Reches, Z., Weinberger, R., Scott, T.E., 1997b. Non-linear elastic behaviour of damaged rocks. Geophysical Journal International 130, 157–166.
Manogharan, P., Wood, C., Marone, C., Elsworth, D., Rivière, J., Shokouhi, P., 2021. Nonlinear elastodynamic behavior of intact and fractured rock under in-situ stress and saturation conditions. Journal of the Mechanics and Physics of Solids 153, 104491.
Manogharan, P., Wood, C., Marone, C., Elsworth, D., Rivière, J., Shokouhi, P., 2022. Experimental investigation of elastodynamic nonlinear response of dry intact, fractured and saturated rock. Rock Mechanics and Rock Engineering 55, 2665–2678.
Matlack, K.H., Kim, J.Y., Jacobs, L.J., Qu, J., 2015. Review of second harmonic generation measurement techniques for material state determination in metals. Journal of Nondestructive Evaluation 34, 273.
McCall, K., 1994. Theoretical study of nonlinear elastic wave propagation. Journal of Geophysical Research: Solid Earth 99, 2591–2600.
McNamara, D.E., Yeck, W.L., Barnhart, W.D., Schulte-Pelkum, V., Bergman, E., Adhikari, L., Dixit, A., Hough, S., Benz, H.M., Earle, P.S., 2017. Source modeling of the 2015 mw 7.8 nepal (gorkha) earthquake sequence: Implications for geodynamics and earthquake hazards. Tectonophysics 714, 21–30.
Meurer, T., Qu, J., Jacobs, L., 2002. Wave propagation in nonlinear and hysteretic media—-a numerical study. International Journal of Solids and Structures 39, 5585–5614.
Moczo, P., Bard, P.Y., 1993. Wave diffraction, amplification and differential motion near strong lateral discontinuities. Bulletin of the Seismological Society of America 83, 85–106.
Murnaghan, F.D., 1937. Finite deformations of an elastic solid. American Journal of Mathematics 59, 235–260.
Narayan, J.P., Sahar, D., 2014. Three-dimensional viscoelastic finite-difference code and modelling of basement focusing effects on ground motion characteristics. Computational Geosciences 18, 1023–1047.
Niu, Z., Gabriel, A.A., Seelinger, L., Igel, H., 2024. Modeling and quantifying parameter uncertainty of co-seismic non-classical nonlinearity in rocks. Journal of Geophysical Research: Solid Earth 129, e2023JB027149.
Nur, A., 1971. Effects of stress on velocity anisotropy in rocks with cracks. Journal of Geophysical Research 76, 2022–2034.
Nur, A., Simmons, G., 1969. Stress-induced velocity anisotropy in rock: An experimental study. Journal of Geophysical Research 74, 6667–6674.
Oeser, J., Bunge, H.P., Mohr, M., 2006. Cluster design in the earth sciences tethys, in: International conference on high performance computing and communications, Springer. pp. 31–40.
Olsen, K., Day, S., Bradley, C., 2003. Estimation of q for long-period (¿ 2 sec) waves in the los angeles basin. Bulletin of the Seismological Society of America 93, 627–638.
Oral, E., Ayoubi, P., Ampuero, J.P., Asimaki, D., Bonilla, L.F., 2022. Kathmandu basin as a local modulator of seismic waves: 2-d modelling of non-linear site re-

sponse under obliquely incident waves. Geophysical Journal International 231, 1996–2008.

Panteleev, I., Lyakhovsky, V., Shalev, E., 2024. Azimuthal pore pressure response to teleseismic waves: effects of damage and stress anisotropy. Geophysical Journal International , ggae081.

Poupinet, G., Ellsworth, W., Frechet, J., 1984. Monitoring velocity variations in the crust using earthquake doublets: An application to the Calaveras Fault, California. Journal of Geophysical Research: Solid Earth 89, 5719–5731.

de la Puente, J., Käser, M., Dumbser, M., Igel, H., 2007. An arbitrary high-order discontinuous Galerkin method for elastic waves on unstructured meshes-IV. Anisotropy. Geophysical Journal International 169, 1210–1228.

Qin, L., Ben-Zion, Y., Bonilla, L.F., Steidl, J.H., 2020. Imaging and monitoring temporal changes of shallow seismic velocities at the Garner Valley near Anza, California, following the M 7.2 2010 El Mayor-Cucapah earthquake. Journal of Geophysical Research: Solid Earth 125, e2019JB018070.

Qiu, H., Hillers, G., Ben-Zion, Y., 2020. Temporal changes of seismic velocities in the San Jacinto Fault zone associated with the 2016 M_W 5.2 Borrego Springs earthquake. Geophysical Journal International 220, 1536–1554.

Rajaure, S., Asimaki, D., Thompson, E.M., Hough, S., Martin, S., Ampuero, J., Dhital, M., Inbal, A., Takai, N., Shigefuji, M., et al., 2017. Characterizing the Kathmandu Valley sediment response through strong motion recordings of the 2015 Gorkha earthquake sequence. Tectonophysics 714, 146–157.

Reinarz, A., Charrier, D.E., Bader, M., Bovard, L., Dumbser, M., Duru, K., Fambri, F., Gabriel, A.A., Gallard, J.M., Köppel, S., et al., 2020. Exahype: an engine for parallel dynamically adaptive simulations of wave problems. Computer Physics Communications 254, 107251.

Remillieux, M.C., Ulrich, T., Goodman, H.E., Ten Cate, J.A., 2017. Propagation of a finite-amplitude elastic pulse in a bar of berea sandstone: A detailed look at the mechanisms of classical nonlinearity, hysteresis, and nonequilibrium dynamics. Journal of Geophysical Research: Solid Earth 122, 8892–8909.

Renaud, G., Le Bas, P.Y., Johnson, P., 2012. Revealing highly complex elastic nonlinear (anelastic) behavior of earth materials applying a new probe: Dynamic acoustoelastic testing. Journal of Geophysical Research: Solid Earth 117.

Rivière, J., Shokouhi, P., Guyer, R.A., Johnson, P.A., 2015. A set of measures for the systematic classification of the nonlinear elastic behavior of disparate rocks. Journal of Geophysical Research: Solid Earth 120, 1587–1604.

Roten, D., Olsen, K., Day, S., Cui, Y., Fäh, D., 2014. Expected seismic shaking in Los Angeles reduced by San Andreas fault zone plasticity. Geophysical Research Letters 41, 2769–2777.

Roten, D., Olsen, K., Pechmann, J., 2012. 3D simulations of M 7 earthquakes on the Wasatch fault, Utah, Part II: Broadband (0–10 Hz) ground motions and nonlinear soil behavior. Bulletin of the Seismological Society of America 102, 2008–2030.

Roten, D., Olsen, K.B., Day, S.M., Cui, Y., 2016. High-frequency nonlinear simulations of southern San Andreas earthquake scenarios. Poster Presentation at 2016 SCEC Annual Meeting.

Roten, D., Yeh, T.Y., Olsen, K.B., Day, S.M., Cui, Y., 2023. Implementation of Iwan-type nonlinear rheology in a 3D high-order staggered-grid finite-difference method. Bulletin of the Seismological Society of America 113, 2275–2291.

Schaff, D.P., Beroza, G.C., 2004. Coseismic and postseismic velocity changes measured by repeating earthquakes. Journal of Geophysical Research: Solid Earth 109.

Sens-Schönfelder, C., Wegler, U., 2006. Passive image interferometry and seasonal variations of seismic velocities at Merapi Volcano, Indonesia. Geophysical research letters 33.

Seylabi, E., Restrepo, D., Taborda, R., Asimaki, D., 2021. Deterministic ground motion simulations with shallow crust nonlinearity at garner valley in southern california. Earthquake Engineering & Structural Dynamics 50, 43–59.

Shah, A., Ribakov, Y., 2009. Non-linear ultrasonic evaluation of damaged concrete based on higher order harmonic generation. Materials & design 30, 4095–4102.

Sharma, M., 2010. Wave propagation in a pre-stressed anisotropic generalized thermoelastic medium. Earth, planets and space 62, 381–390.

Shokouhi, P., Rivière, J., Guyer, R.A., Johnson, P.A., 2017. Slow dynamics of consolidated granular systems: Multi-scale relaxation. Applied Physics Letters 111, 251604.

Stanzione, D., West, J., Evans, R.T., Minyard, T., Ghattas, O., Panda, D.K., 2020. Frontera: The evolution of leadership computing at the National Science Foundation, in: Practice and Experience in Advanced Research Computing 2020: Catch the Wave, Association for Computing Machinery. pp. 106–111. URL: https://doi.org/10.1145/3311790.3396656, doi:10.1145/3311790.3396656.

Taborda, R., Roten, D., 2015. Physics-based ground-motion simulation. Encyclopedia of Earthquake Engineering, Springer-Verlag, Berlin Heidelberg .

Takai, N., Shigefuji, M., Rajaure, S., Bijukchhen, S., Ichiyanagi, M., Dhital, M.R., Sasatani, T., 2016. Strong ground motion in the Kathmandu Valley during the 2015 Gorkha, Nepal, earthquake. Earth, Planets and Space 68, 1–8.

Taufiqurrahman, T., Gabriel, A.A., Ulrich, T., Valentova, L., Gallovič, F., 2022. Broadband dynamic rupture modeling with fractal fault roughness, frictional heterogeneity, viscoelasticity and topography: The 2016 Mw 6.2 Amatrice, Italy earthquake. Geophysical Research Letters 49, e2022GL098872.

Tinti, E., Spudich, P., Cocco, M., 2005. Earthquake fracture energy inferred from kinematic rupture models on extended faults. Journal of Geophysical Research: Solid Earth 110.

Titarev, V.A., Toro, E.F., 2002. Ader: Arbitrary high order Godunov approach. Journal of Scientific Computing 17, 609–618.

Toro, E.F., Millington, R., Nejad, L., 2001. Towards very high order Godunov schemes, in: Godunov methods: theory and applications, Springer. pp. 907–940.

Uphoff, C., 2020. Flexible model extension and optimisation for earthquake simulations at extreme scales. Ph.D. thesis. Technische Universität München.

Uphoff, C., Bader, M., 2016. Generating high performance matrix kernels for earthquake simulations with viscoelastic attenuation, in: 2016 international conference on high performance computing & simulation (HPCS), IEEE. pp. 908–916.

Uphoff, C., Krenz, L., Ulrich, T., Wolf, S., Schneller, D., Kurapati, V., Knoll, A., Li, D., Dorozhinskii, R., Heinecke, A., Wollherr, S., Bohn, M., Schliwa, N., Brietzke, G., Taufiqurrahman, T., Anger, S., Rettenberger, S., Simonis, F., Gabriel, A., Pauw, V., Breuer, A., Kutschera, F., Hendrawan Palgunadi, K., Rannabauer, L., van de Wiel, L., Li, B., Chamberlain, C., Yun, J., Rekoske, J., G, Y., Bader, M., 2024. SeisSol. URL: https://doi.org/10.5281/zenodo.14051105, doi:10.5281/zenodo.14051105.

Uphoff, C., Rettenberger, S., Bader, M., Madden, E.H., Ulrich, T., Wollherr, S., Gabriel, A.A., 2017. Extreme Scale Multi-physics Simulations of the Tsunamigenic 2004 Sumatra Megathrust Earthquake, in: Proceedings of the International Conference for High Performance Computing, Networking, Storage and Analysis, ACM, New York, NY, USA. pp. 21:1–21:16. doi:10.1145/3126908.3126948.

Vardanega, P.J., Bolton, M.D., 2013. Stiffness of clays and silts: Normalizing shear modulus and shear strain. Journal of Geotechnical and Geoenvironmental Engineering 139, 1575–1589.

Wang, S.Y., Zhuang, H.Y., Zhang, H., He, H.J., Jiang, W.P., Yao, E.L., Ruan, B., Wu, Y.X., Miao, Y., 2021. Near-surface softening and healing in eastern Honshu associated with the 2011 magnitude-9 Tohoku-Oki Earthquake. Nature communications 12, 1–10.

Wei, S., Chen, M., Wang, X., Graves, R., Lindsey, E., Wang, T., Karakaş, Ç., Helmberger, D., 2018. The 2015 Gorkha (Nepal) earthquake sequence: I. Source modeling and deterministic 3D ground shaking. Tectonophysics 722, 447–461.

Wilcox, L.C., Stadler, G., Burstedde, C., Ghattas, O., 2010. A high-order discontinuous galerkin method for wave propagation through coupled elastic–acoustic media. Journal of computational Physics 229, 9373–9396.

Wolf, S., Galis, M., Uphoff, C., Gabriel, A.A., Moczo, P., Gregor, D., Bader, M., 2022. An efficient ader-dg local time stepping scheme for 3d hpc simulation of seismic waves in poroelastic media. Journal of Computational Physics 455, 110886.

Wollherr, S., Gabriel, A.A., Mai, P.M., 2019. Landers 1992 "reloaded": Integrative dynamic earthquake rupture modeling. Journal of Geophysical Research: Solid Earth 124, 6666–6702.

Wollherr, S., Gabriel, A.A., Uphoff, C., 2018. Off-fault plasticity in three-dimensional dynamic rupture simulations using a modal Discontinuous Galerkin method on unstructured meshes: implementation, verification and application. Geophysical Journal International 214, 1556–1584.

Youssef, I.K., El-Arabawy, H., 2007. Picard iteration algorithm combined with Gauss–Seidel technique for initial value problems. Applied Mathematics and computation 190, 345–355.